

ASD/OCD-Linked Protocadherin-10 Regulates Synapse, But Not Axon, Development in the Amygdala and Contributes to Fear- and Anxiety-Related Behaviors

Naosuke Hoshina,¹ Erin M. Johnson-Venkatesh,¹ Veronica R. Rally,¹ Jaanvi Sant,¹ Miyuki Hoshina,¹ Mariel P. Seiglie,¹ and Hisashi Umemori¹

Department of Neurology, F.M. Kirby Neurobiology Center, Boston Children's Hospital, Harvard Medical School, Boston, Massachusetts 02115

The *Protocadherin-10* (*PCDH10*) gene is associated with autism spectrum disorder (ASD), obsessive-compulsive disorder (OCD), and major depression (MD). The PCDH10 protein is a homophilic cell adhesion molecule that belongs to the $\delta 2$ -protocadherin family. PCDH10 is highly expressed in the developing brain, especially in the basolateral nucleus of the amygdala (BLA). However, the role of PCDH10 *in vivo* has been debatable: one paper reported that a *Pcdh10* mutant mouse line showed changes in axonal projections; however, another *Pcdh10* mutant mouse line was reported to have failed to detect axonal phenotypes. Therefore, the actual roles of PCDH10 in the brain remain to be elucidated. We established a new *Pcdh10* KO mouse line using the CRISPR/Cas9 system, without inserting gene cassettes to avoid nonspecific effects, examined the roles of PCDH10 in the brain, and studied the behavioral consequences of *Pcdh10* inactivation. Here, we show that *Pcdh10* KO mice do not show defects in axonal development. Instead, we find that *Pcdh10* KO mice exhibit impaired development of excitatory synapses in the dorsal BLA. We further demonstrate that male *Pcdh10* KO mice exhibit reduced anxiety-related behaviors, impaired fear conditioning, decreased stress-coping responses, and mildly impaired social recognition and communication. These results indicate that PCDH10 plays a critical role in excitatory synapse development, but not axon development, in the dorsal BLA and that PCDH10 regulates anxiety-related, fear-related, and stress-related behaviors. Our results reveal the roles of PCDH10 in the brain and its relationship to relevant psychiatric disorders such as ASD, OCD, and MD.

Key words: autism spectrum disorder; basolateral nucleus of the amygdala; fear and anxiety; obsessive-compulsive disorder; PCDH10; synapse development

Significance Statement

Protocadherin-10 (*PCDH10*) encodes a cell adhesion molecule and is implicated in autism spectrum disorder (ASD), obsessive-compulsive disorder (OCD), and major depression (MD). PCDH10 is highly expressed in the basolateral nucleus of the amygdala (BLA). However, the phenotypes of previously published *Pcdh10* mutant mice are debatable, and some are possibly because of the nonspecific effects of the *LacZ/Neo* cassette inserted in the mice. We have generated a new *Pcdh10* mutant mouse line without the *LacZ/Neo* cassette. Using our new mouse line, we reveal the roles of PCDH10 for excitatory synapse development in the BLA. The mutant mice exhibit anxiety-related, fear-related, and stress-related behaviors, which are relevant to ASD, OCD, and MD, suggesting a possible treatment strategy for such psychiatric disorders.

Received Sep. 11, 2021; revised Mar. 14, 2022; accepted Mar. 17, 2022.

Author contributions: N.H. and H.U. designed research; N.H., E.M.J.-V., V.R.R., J.S., M.H., and M.P.S. performed research; N.H., E.M.J.-V., V.R.R., and H.U. analyzed data; N.H. and H.U. wrote the first draft of the paper; N.H., E.M.J.-V., and H.U. edited the paper; N.H., E.M.J.-V., and H.U. wrote the paper.

This work was supported by the National Institutes of Health (NIH)/National Institute on Drug Abuse Grant DA042744, the NIH/National Institute of Mental Health Grant MH125162, and the Simons Foundation Autism Research Initiative (SFARI) Grant 568285 (to H.U.) and the Uehara Memorial Foundation overseas postdoctoral research fellowship (N.H.). We thank the Mouse Gene Manipulation Core and Neurodevelopmental Behavioral Core at Boston Children's Hospital for technical contributions. We also thank A. Das for mouse colony management.

The authors declare no competing financial interests.

Correspondence should be addressed to Hisashi Umemori at hisashi.umemori@childrens.harvard.edu.

<https://doi.org/10.1523/JNEUROSCI.1843-21.2022>

Copyright © 2022 the authors

Introduction

Autism spectrum disorder (ASD) is a developmental disorder characterized by difficulties with social skills, problems with speech and communication, and repetitive behaviors. It often co-occurs with other medical conditions such as anxiety disorders, mood disorders, and obsessive-compulsive disorder (OCD). There are substantial similarities and overlaps in the etiology and pathophysiology among these disorders, such as synaptic changes in the brain (Lima Caldeira et al., 2019). However, the molecular and neural circuit basis of ASD and co-occurring conditions still remains to be elucidated.

ASD is associated with a combination of genetic and environmental factors (Chaste and Leboyer, 2012). Various human genes are implicated in ASD susceptibility. One of them is the *Protocadherin-10* (*PCDH10*) gene (Toro et al., 2010; SFARI, Score 3). Homozygous deletions in the regulatory region of the *PCDH10* gene and copy number variants of the *PCDH10* gene have been found in ASD patients (Morrow et al., 2008; Bucan et al., 2009). The *PCDH10* gene is also implicated in OCD. Whole-genome association analysis showed that *PCDH10* variations are linked to SSRI (selective serotonin reuptake inhibitor) treatment response in OCD (Qin et al., 2016). In addition, *PCDH10* is identified as one of the genes associated with major depression (MD; Roberson-Nay et al., 2020). Thus, investigating the role of PCDH10 and the neural circuits and behavior regulated by PCDH10 will shed light on the understanding of ASD and co-occurring conditions.

The *PCDH10* gene encodes a single transmembrane protein that belongs to the δ 2-protocadherin family (Redies et al., 2005). PCDH10 mediates calcium-dependent cell-cell adhesion by homophilic binding through its extracellular cadherin (EC) domains. In culture, PCDH10 has been shown to regulate contact-mediated cell migration (Nakao et al., 2008) and MEF2 (myocyte enhancer factor 2)-mediated synapse elimination (Tsai et al., 2012). In contrast, the role of PCDH10 *in vivo* is debatable. One paper reported that a homozygous *Pcdh10* mutant (*Pcdh10*^{LacZ/Neo} KO) line, in which a *LacZ/Neo* cassette was inserted to disrupt the first exon of the *Pcdh10* gene, showed changes in axonal projections, including striatal and thalamocortical projections (Uemura et al., 2007). Heterozygous *Pcdh10*^{LacZ/Neo} mice showed sociability defects (Schoch et al., 2017) and altered γ oscillations (Port et al., 2017). In addition, *Pcdh10*^{LacZ/Neo} KO mice are postnatally lethal. However, a review paper stated that analysis of another *Pcdh10* KO mouse line, which was generated independently, failed to detect axonal growth phenotypes (Hayashi and Takeichi, 2015). We posit that the axonal defects of the homozygous *Pcdh10*^{LacZ/Neo} mice are possibly because of the *LacZ/Neo* cassette inserted into the mouse line. This is based on an earlier *Pcdh17* KO mouse line that we generated. We first generated *Pcdh17*^{LacZ/Neo} mice, in which a *LacZ/Neo* cassette was inserted to disrupt the first exon of the *Pcdh17* gene (Hoshina et al., 2013, see their Fig. S3). We found that this line showed various brain abnormalities including striatal axonal growth defects. However, after removing the *LacZ/Neo* cassette, the striatal axonal growth phenotypes were no longer observed (Hoshina et al., 2013, see their Fig. S3), suggesting that the *LacZ/Neo* cassette had nonspecific effects on axon targeting. Therefore, the precise roles of PCDH10 in the brain remain to be elucidated.

Here, we generated a new *Pcdh10* KO mouse line, which does not have a *LacZ/Neo* cassette, to re-evaluate the role of PCDH10 in the brain. Our *Pcdh10*^{-/-} mice are not lethal and do not show defects in striatal axonal growth. Instead, we found defects in synapse development in the BLA, where PCDH10 is highly expressed. Consistently, our *Pcdh10*^{-/-} mice showed altered anxiety and fear conditioning, which require BLA function. *Pcdh10*^{-/-} mice also appear to show changes in social recognition and social communication, although sociability seemed normal. Our results reveal that the role of PCDH10 is in synapse, but not axon, development. Furthermore, our results demonstrate the importance of PCDH10 in the regulation of anxiety, fear, and social recognition/communication, which is consistent with the involvement of PCDH10 in ASD and co-occurring conditions.

Materials and Methods

Antibodies

Rabbit polyclonal anti-PCDH10 antibodies against amino acids 728–932 of the PCDH10 protein (Antigen site 1) were described previously (Hoshina et al., 2013). Rabbit polyclonal anti-PCDH10 antibodies against amino acids 1008–1040 of the PCDH10 protein (Antigen site 2) were generated using the methods described before (Hoshina et al., 2013). Rat polyclonal anti-PCDH10 antibodies against Antigen site 1 were also generated using the same methods (Hoshina et al., 2013), except rats were used for immunization to obtain antiserum. The specificity of the PCDH10 antibodies was confirmed using *Pcdh10* KO mice. The PCDH10 antibodies were used at 1–4 μ g/ml. The following primary antibodies were also used: mouse anti- β -catenin (1:500; BD Transduction Laboratories; 610153), mouse anti-DARPP-32 (Dopamine and cAMP-regulated phosphoprotein 32 kDa; 1:1000; BD Transduction Laboratories; 611520), mouse anti-tyrosine hydroxylase (TH; 1:1000; MilliporeSigma; MAB5280), mouse anti-neurofilament (1:2000; Covance; SMI-312R), rabbit anti-neurofilament (1:2000; MilliporeSigma; N4142), mouse anti-MAP2 (Microtubule-associated protein 2; 1:500; MilliporeSigma; M4403), guinea pig anti-VGLUT1 (Vesicular glutamate transporter 1; 1:5000; Millipore; AB5905), guinea pig anti-VGLUT2 (Vesicular glutamate transporter 2; 1:1000; Frontier Institute; Af810), rabbit anti-VGAT (Vesicular GABA Transporter; 1:1000; Synaptic Systems; 131003), mouse anti-PSD95 (1:500; MilliporeSigma; CP35), mouse anti-PSD95 (1:500; NeuroMab; 75-028), and mouse anti-gephyrin (1:500; Synaptic Systems; 147021). The following secondary antibodies (Jackson ImmunoResearch) were used for immunoblotting: horseradish peroxidase (HRP)-conjugated goat anti-rabbit IgG (111-035-003) and HRP-conjugated goat anti-mouse IgG (115-035-003). The following secondary antibodies (Thermo Fisher Scientific) were used for immunohistochemistry: donkey anti-rabbit IgG, Alexa Fluor 488 (A-21206), donkey anti-mouse IgG, Alexa Fluor 488 (A-21202), Alexa Fluor 568 (A10037), Alexa Fluor 647 (A-31571), goat anti-guinea pig IgG, Alexa Fluor 488 (A-11073), Alexa Fluor 568 (A-11075), and goat anti-rat IgG, Alexa Fluor 647 (A-21247).

Animals

Pcdh10 mutant mice were generated in our laboratory. *Thy1-GFP-M* mice (The Jackson Laboratory; 007788) were described previously (Feng et al., 2000). Mice were maintained in standard housing conditions on a 12/12 h light/dark cycle with food and water provided *ad libitum*. All animal care and use were in accordance with the institutional guidelines and approved by the Institutional Animal Care and Use Committees at Boston Children's Hospital.

Generation of *Pcdh10* mutant mice

Pcdh10 mutant mice were generated using the CRISPR/Cas9 system. Two gRNAs were designed so that the first exon of *Pcdh10* would be deleted after cleavage. gRNA target sequences including the PAM sequence (italic) were 5'-CTCCTTTATFCCGACAGTGTGG-3' and 5'-GAGGGCCAATCACTGACAAAGG-3'. crRNA and tracrRNA were from MilliporeSigma. They were injected with Cas9 proteins into the pronucleus of fertilized zygotes (C57BL/6N), and the injected zygotes were transferred into oviducts of pseudo-pregnant female mice. The pups were tested for the deletion of the first exon of the *Pcdh10* gene by genomic PCR. Wild-type and *Pcdh10* mutant (null) alleles were detected by PCR assays in which primer P1 (5'-GCTCGCGTTTGCCAGCCGTTGATATC-3') and primer P2 (5'-GCTCAGCCGTAATCTTCCC ACTGACC-3') amplified a wild-type fragment and primer P1 and primer P3 (5'-ACTGGTACACGCGACTGAAAACAGTG-3') amplified a mutant fragment. The absence of PCDH10 proteins was also confirmed by immunoblotting and immunostaining. *Pcdh10* mutant mice were backcrossed with C57BL/6 mice and maintained on a C57BL/6 background.

Immunohistochemistry

Male and female mouse brains were perfused with 4% paraformaldehyde (PFA) in PBS, postfixed in 4% PFA in PBS overnight at 4°C, and then cryoprotected in 30% sucrose in PBS at 4°C. For

PCDH10 staining, mouse brains were perfused with 2% PFA in PBS without postfixation. Brains were frozen and sectioned at 16- μ m thickness on a CM3050S cryostat (Leica). For PSD95 and gephyrin staining, sections were pretreated with 1 mg/ml pepsin in 0.2 N HCl for 10 min at room temperature before staining. Sections were incubated with blocking buffer (2% BSA/2% goat serum/0.1% Triton X-100 in PBS) for 1 h at room temperature, incubated with primary antibodies in blocking buffer overnight at 4°C, and incubated with fluorescent secondary antibodies (1:500; Thermo Fisher Scientific) in blocking buffer for 2 h at room temperature. Sections were washed with PBS between incubation steps. Sections were mounted with Fluoromount-G.

Imaging

Images were taken with a BZ-X810 fluorescence microscope (Keyence) or an LSM700 confocal microscope (Zeiss). Images were obtained with the identical acquisition settings regarding the exposure time, laser power, detector gain, and amplifier offset. For wide-field imaging with a BZ-X810 fluorescence microscope, images were obtained by stitching several adjacent images together. The average signal intensity was quantified using ImageJ. The ROIs analyzed are as follows: the total area of the striatum, GPe, GPI, and SNr (DARPP-32); the total area of the striatum (TH); the total area of the cerebral cortex, striatum, internal capsule, and thalamus (neurofilament); the total area of the ec (external capsula: cortical input axons) and ic (internal capsula: thalamic input axons; neurofilament); the total area of the BLA (MAP2); and the total area of the dorsal BLA and ventral BLA (VGLUT1, VGLUT2, VGAT). For images with DARPP-32 and TH staining, the signal intensity in the corpus callosum was calculated as the background signal. For images with neurofilament and MAP2 staining, the signal intensity in the fiber-poor regions in the striatum and the internal capsule, respectively, were calculated as the background signal. For images with VGLUT1, VGLUT2, and VGAT staining, the signal intensity in the optic nerve was calculated as the background signal. The background signals were subtracted from the signal intensities in the ROIs. The mean value of the background-subtracted signal intensities was calculated from *Pcdh10*^{+/+} mice. This mean intensity was set as 100%. All data points of the background-subtracted signal intensities from *Pcdh10*^{+/+} and *Pcdh10*^{-/-} mice were then normalized to the mean value, expressed as the percentage relative to the mean from *Pcdh10*^{+/+} mice (%+/+), and plotted in the graphs. For colocalization experiments, confocal images at 1024 × 1024 pixels were acquired as a single plane using a 63× objective lens with a 2.0× zoom. % colocalization of synaptic marker proteins with PCDH10 was quantified using ImageJ (Hoshina et al., 2021). The background intensity was calculated and subtracted from images using the Auto Threshold plugin. For % colocalization analysis, background-subtracted binary images were prepared, and the PCDH10 binary image was overlaid onto the synaptic protein image (“actual”). For correlation analysis, the 180°-rotated PCDH10 image was overlaid onto the synaptic protein image (“rotated”). Puncta were considered colocalized if >10% of a PCDH10 punctum was overlapped with a synaptic punctum (Hoshina et al., 2021). The total number of synaptic puncta and the number of PCDH10-colocalized synaptic puncta were counted, and % colocalization was calculated. Puncta smaller than 6 pixels were excluded from analysis. Colocalization of PSD95 and VGLUT1 was quantified using ImageJ. The background intensity was calculated and subtracted from images using the Auto Threshold plugin. Background-subtracted binary images were prepared, and the PSD95 binary image was overlaid onto the VGLUT1 binary image. The total number of PSD95 puncta and the number of PSD95 puncta with VGLUT1 puncta were counted, and % of PSD95 puncta with VGLUT1 puncta was calculated. In the same way, the total number of VGLUT1 puncta and the number of VGLUT1 puncta with PSD95 puncta were counted, and % of PSD95 puncta with VGLUT1 puncta was calculated. For confocal imaging of VGLUT1, VGLUT2, VGAT, PSD95, and gephyrin staining, images at 1024 × 1024 pixels were acquired as a z-stack (12 optical sections, 0.5- μ m step size) using a 63× objective lens with a 1.0× zoom. The signal intensity in the optic nerve was calculated as the background signal and subtracted from

each image. The density and size of puncta were quantified using ImageJ. Puncta smaller than six pixels were excluded from analysis.

Imaging of axons and spines

For the imaging of axon fibers of the hippocampus-BLA projections and BLA dendritic spines, *Thy1-GFP-M;Pcdh10* male littermates at four-week-old were perfused with 4% PFA in PBS. Brains were removed, postfixed in 4% PFA in PBS overnight at 4°C, and cryoprotected in 30% sucrose in PBS at 4°C; 60- μ m-thick sections were cut on a CM3050S cryostat and collected in PBS. Sections were washed with PBS and then mounted with Fluoromount-G. Images of GFP fluorescence were taken with an LSM700 confocal microscope. Images at 1024 × 1024 pixels were acquired as a z-stack (for axon fibers, 7–10 optical sections, 7- μ m step size; for dendritic spines, 11 optical sections, 0.5- μ m step size) using a 25× objective lens with a 0.5× zoom (axon fibers) or a 63× objective lens with a 2.0× zoom (dendritic spines). Images were obtained with the identical acquisition settings regarding the exposure time, detector gain, and amplifier offset. The number of GFP-labeled hippocampus-BLA projections and the number of axon bundles in the distal regions of hippocampus-BLA axons were quantified using ImageJ. For this, the signal intensity in the GFP negative areas of the image was calculated as the background signal. For the number of GFP-labeled axons, the GFP fluorescence intensity along the dotted line drawn on the bundles of axon fibers was analyzed. The number of GFP signal peaks was counted after background signal subtraction. For the number of axon bundles in the distal regions, the GFP fluorescence intensity along the solid line at a 200- μ m distance from the medial edge of the BLA was analyzed. Axonal signals with three consecutive peaks within 20 μ m were considered to be one axonal bundle (Zhu et al., 2016). Analyses of dendritic spines were performed by an individual blind to the genotype. The number of dendritic spines in the image was counted manually. The number of dendritic spines was divided by the dendrite length to calculate the density. Spines were classified into the following categories according to previous reports (Sorra and Harris, 2000; Johnson-Venkatesh et al., 2015): (1) Filopodia, where the neck length was >1.5 μ m; (2) Thin, where the head width was <0.5 μ m; (3) Mushroom, where the head width was >0.5 μ m; and (4) Stubby, where the neck was absent.

Fluorescent *in situ* hybridization

Fluorescent *in situ* hybridization was performed with an RNAscope Fluorescent Multiplex kit (Advanced Cell Diagnostics). Mm-*Pcdh10* (Advanced Cell Diagnostics; 477781) was used as the RNAscope probe. Mice were decapitated, and their brains were removed and immediately frozen. Brains were sectioned at 16- μ m thickness on a CM3050S cryostat and mounted onto Superfrost Plus slides (Thermo Fisher Scientific). Sections were fixed with prechilled 4% PFA in PBS for 15 min at 4°C, rinsed in PBS, dehydrated in an ethanol dilution series, and air-dried for 10 min. A hydrophobic barrier was drawn around each section with an ImmEdge barrier pen. Sections were then pretreated with Protease III for 30 min at room temperature, incubated with the RNAscope probe for 2 h at 40°C in a HybEZ oven, and treated with amplifier and fluorescently labeled probes (AMP1 for 30 min at 40°C; AMP2 for 15 min at 40°C; AMP3 for 30 min at 40°C; AMP4 AltC for 15 min at 40°C). Sections were washed with 1× Wash Buffer between the incubation steps. Sections were mounted with Fluoromount-G. Images were taken with a BZ-X810 fluorescence microscope.

Immunoblotting

Male and female mouse brains were homogenized in lysis buffer (50 mM Tris-HCl pH 7.4, 150 mM NaCl, 5 mM EDTA, and 1% Triton X-100). Lysates were resolved by SDS-PAGE and transferred to polyvinylidene difluoride membranes (Bio-Rad). Membranes were blocked with 3% milk/0.1% Tween 20 in Tris-buffered saline for 1 h at room temperature and blotted with primary antibodies overnight at 4°C followed by HRP-conjugated secondary antibodies (1:5000; Jackson ImmunoResearch) for 1 h at room temperature. Western ECL Substrate (Bio-Rad) was used to visualize the immunoreactive proteins with ImageQuant LAS 4000 (GE Healthcare) and Kwik Quant Imager (Kindle Biosciences LLC).

Electrophysiology

All electrophysiological experiments and analyses were done blind. For miniature EPSC (mEPSC) and mIPSC recordings, acute amygdaloid slices were prepared from *Pcdh10* littermate male and female mice at four- to five-week-old. Mice were anesthetized with isoflurane, decapitated, and their brains were removed; 300- μ m coronal slices were cut using a VT1200S vibratome (Leica). Slices were cut in an ice-cold solution (206 mM sucrose, 2.8 mM KCl, 2 mM MgSO₄, 1 mM MgCl₂, 1.25 mM NaH₂PO₄, 1 mM CaCl₂, 10 mM glucose, 26 mM NaHCO₃, and 0.4 mM ascorbic acid). Slices were then put into artificial CSF (aCSF; 127 mM NaCl, 1.6 mM KCl, 1.24 mM KH₂PO₄, 1.3 mM MgSO₄, 2.4 mM CaCl₂, 10 mM glucose, and 26 mM NaHCO₃) for 1 h at room temperature. All solutions were continuously bubbled with 95% O₂/5% CO₂. Neurons were visualized using a customized Scientific/Olympus microscope. Data were obtained with a Multiclamp 700B amplifier (Molecular Devices), digitized with Digidata 1440A (Molecular Devices), and collected with Clampex 10.7 (Molecular Devices). Whole-cell patch-clamp recordings were conducted with 4- to 6-M Ω pipette containing (for mEPSCs) 135 mM K-gluconate, 4 mM KCl, 10 mM HEPES, 4 mM Mg-ATP, 0.3 mM Na₂-GTP, 10 mM Na₂-phosphocreatine, and 0.15% Lucifer yellow. pH was adjusted to 7.2–7.3 with KOH. For mIPSCs, pipettes contained: 135 mM CsCl₂, 1 mM EGTA, 5 mM MgCl₂, 4 mM ATP, 1 mM GTP, and 10 mM HEPES (pH 7.2). Cells were held at -70 mV. aCSF was supplemented during recordings with 500 nM tetrodotoxin and 50 μ M picrotoxin (for mEPSC recordings) or 10 μ M CNQX and 25 μ M APV (for mIPSCs) and warmed to 32°C. mEPSCs and mIPSCs were analyzed using MiniAnalysis (Synaptosoft).

Behavioral tests

All data acquisition and analyses were conducted by an individual blind to the genotype. Two- to four-month-old male mice were used for experiments as previously described (Hoshina et al., 2013; Williams et al., 2016; Terauchi et al., 2017). Because female mice have estrous cycles that may result in more behavioral variabilities than male mice (Chari et al., 2020), we used male mice in the behavioral studies.

Repetitive behaviors

Mice were placed in a clean, empty mouse cage without bedding that was illuminated at 2 lux. Mice were given a 10 min habituation period in the cage, and then for the next 10 min, cumulative time spent grooming all body regions and rearing numbers were quantified. Behaviors were recorded from 7 to 9 P.M. (at the initiation of the dark cycle) with a handycam camera (Panasonic HDC-SD60). Grooming duration and rearing numbers were manually calculated.

Open field test

Mice were placed in the center of an open-field apparatus [41 × 41 × 38 cm (W × D × H)] illuminated at 30 lux and allowed to move freely for 15 min. Distance traveled for each 1 min, total distance traveled, and time spent in the center area [26 × 26 cm (~40% of the total area)] were recorded and analyzed with EthoVision XT software (Noldus).

Elevated plus maze test

The elevated plus maze consisted of two open arms and two closed arms of the same size (35 × 6 cm) extending from the central area (6 × 6 cm). The maze was elevated 75 cm from the ground and illuminated at 3 lux. Mice were placed in the central square of the maze facing one of the open arms and allowed to move for 10 min. Times spent in the open arm, closed arm, and center area were recorded and analyzed with EthoVision XT software.

Light-dark transition test

The light-dark box consisted of two compartments: a white (light) box without a lid (500 lux) and a black (dark) box (both 25 × 25 × 25 cm). The two boxes were separated by a vertical sliding door that remained open (4 × 6 cm). Mice were placed in the black box and allowed to move between boxes for 10 min. Times spent in the light box and dark box, and the transition between boxes were recorded and analyzed with EthoVision XT software.

Tail suspension test

Mice were suspended above the floor by taping the end of their tails to the top side of a box, and their behaviors were recorded with a handycam camera. Total immobility time over 6 min and immobility time during each 1-min bin were manually calculated.

Forced swim test

Mice were placed in a cylinder filled with water (~22°C), and their behaviors were recorded with a handycam camera. Total immobility time in 10 min trial and immobility time during each 2-min bin were manually calculated.

Contextual and auditory fear conditioning tests

The fear conditioning test was conducted in a small conditioning chamber surrounded by a sound-attenuating chest (Ugo Basile). On day 1, mice were placed in the conditioning chamber (a square box with four vertical striped wallpapers) for 8 min and then presented with a tone of 10 kHz for 30 s followed by a foot shock (2 s/0.30 mA). The tone and shock were repeated three times with 2-min intervals. On day 2, the mice were placed in the same conditioning chamber for 6 min. On day 3, the mice were placed in a novel chamber with contexts that were different from those of the conditioning chamber (a transparent circular box) for 3 min and then presented with the tone for 3 min. Freezing responses were recorded during the tests and analyzed with EthoVision XT software.

Accelerating rotarod test

Mice were placed on a drum (Columbus Instruments) rotating at 5 rpm at the beginning. The rotation of the rotarod was accelerated to 35 rpm over a 300-s period at a constant rate. The latency to fall off the rotarod was measured. Mice were tested for two consecutive days, receiving three trials per day at intervals of 3 h between trials.

Acoustic startle response (ASR) and prepulse inhibition (PPI) tests

The startle reflex measurement system (Kinder Scientific) was used for assessing ASRs and PPI. A test session began by placing a mouse in a chamber where it was left undisturbed for 5 min. The startle response was recorded for 250 ms starting with the onset of a startle stimulus. The background noise level in the chamber was 60 dB. The peak startle amplitude during the 250-ms sampling window was recorded as a measure of the startle response. ASR test was done on day 1. The intensities of startle stimuli were 60, 70, 80, 90, 100, 110, and 120 dB. PPI test was done on day 2. The prepulse sound was presented 100 ms before the startle stimulus (110 dB), and its intensity was 70, 74, 78, and 82 dB. Each trial was presented in a pseudorandom order. The average intertrial interval (ITI) was 15 s (range, 10–20 s). The following formula was used to calculate % PPI of the startle response: $100 - [100 \times (\text{startle response on prepulse trials} / \text{startle response on 110 dB startle trials})]$.

Social interaction and social recognition tests

Social interaction and social recognition tests were conducted in a three-chambered apparatus [62 × 40 × 22 cm (W × D × H)] with two small cages at the corner of the side chambers. The chamber was illuminated at 3 lux. Habituation, the social interaction test, and the social recognition test were performed in that order. During habituation, mice were placed in the center chamber of the apparatus and allowed to move freely for 10 min. In the social interaction test, a stranger mouse (S) was placed in the left or right corner cage. The test mouse was allowed to explore the stranger mouse (S) and the empty cage (E) freely for 10 min. In the social recognition test, a novel stranger mouse (N) was placed the previously empty cage. The previously stranger mouse (S) became the familiar mouse (F) during this session. The test mouse was allowed to explore the novel stranger mouse (N) and the familiar mouse (F) freely for 10 min. Times spent around the cages by the test mice were recorded and analyzed with EthoVision XT software. For the analysis, the times spent around the cages in the first 5 min of the 10-min test were quantified in both tests. The following formula was used to calculate the social preference index: $(S - E) / (S + E) \times 100$ for the social interaction test and $(N - F) / (N + F) \times 100$ for the social recognition test.

Ultrasonic vocalization (USV) test

Postnatal day (P)6–P8 male pups were separated from their mother and placed alone in a Mouse Opti cage [34 × 29 × 15 cm (W × D × H)] containing clean bedding. Each cage was placed inside of a sound-attenuating chamber (Metris) for 5 min. The chamber was illuminated at 30 lux. USVs were recorded using a Gold Foil Electrostatic Transducer microphone (Metris). Recordings were made with Metris Sonotrack 2 software. The numbers of USVs emitted over 5 min were counted with Metris Sonotrack 2 software.

Hot plat test

The surface of the metal hot plate was heated to a temperature of 52°C, and mice were placed on the hot plate surface. Withdrawal latency was manually counted until the mouse exhibited a nociceptive response, such as a hind paw lick or a jump.

Visual test

The test was conducted in a touchscreen operant chamber, equipped with an infrared touch screen, a black mask with two windows, a liquid dipper, and a reward tray (Lafayette Instrument). Mice could access 10% condensed milk (Borden Sugar Condensed Eagle Brand Milk) as a reward from the reward tray. The operant chamber is controlled using ABET II (Lafayette Instrument) and Whisker (Lafayette Instrument) software. The body weights of mice were slowly reduced and maintained to 85% of free-feeding weight by restricted feeding throughout testing. During restricted feeding, mice could access ~2 g of regular mouse chow per day. The visual test involved three stages. Mice were required to meet a set criterion for each stage before proceeding to the next stage. In stage 1, mice were placed in the chamber for 60 min and exposed to 200 μ l of condensed milk in the reward tray. Once mice had consumed all the milk in 60 min, they proceeded to the next stage. In stage 2, the mice were trained to collect a milk reward (20 μ l each time) from the reward tray, after the following cues: a tone and illumination of the tray light. After the reward was collected, the tray illumination turned off, and a 30-s ITI was initiated before the delivery of the next reward. Mice that successfully completed 30 trials in 60 min proceeded to the next stage. In stage 3, mice were trained to touch visual stimuli that were randomly presented in one of the two spatial locations on the screen. Various shapes were used for the visual stimuli. If mice touch the blank screen, no reward was given. Touching the visual stimulus resulted in its disappearance accompanied by delivery of the reward, a tone, and tray illumination. Reward collection turned off the tray illumination and initiated an ITI of 10 s before the next trial. Mice that successfully completed 30 trials in 60 min were considered to have met the criterion in stage 3. The days to the criterion were quantified.

Experimental design and statistical analysis

Statistical analyses were performed using GraphPad Prism software. The statistical tests performed were two-tailed Student's *t* test, two-way ANOVA, or two-way repeated measured ANOVA as indicated in the results and figure legends. Two-way ANOVA and two-way repeated measured ANOVA were followed by Sidak's *post hoc* test. All data are expressed as mean \pm SEM. Sample sizes (*n*) are indicated in the figure legends. Our sample sizes were similar to those reported in previous publications in the field (Umemori et al., 2004; Hoshina et al., 2013, 2021). Significance was set as **p* < 0.05, ***p* < 0.01, or ****p* < 0.005 for all data. *Post hoc* statistical calculation of sample sizes for behavioral experiments was also done to ensure that sample sizes had sufficient power for subsequent statistical analyses (at least 75% power at the 0.05 level of significance for each set of experiments). Steps in the experiments were randomized to minimize the effects of confounding variables, including how mice were chosen for experiments, order of treatments, etc. Imaging was done in the same fashion among conditions. For quantification, cells and fields from brain sections were chosen randomly from the region of interest. No data points were excluded from any experiments.

Results

Generation of a new *Pcdh10* KO mouse line without a *LacZ/Neo* cassette

To reveal the actual roles of PCDH10 in the brain, we generated a new *Pcdh10* KO mouse line without a *LacZ/Neo* cassette, using the CRISPR/Cas9 system. In order to avoid any interference from the artificial gene insertion, we simply deleted the coding region of exon 1 (Fig. 1A,B), which encodes the extracellular and transmembrane domains of PCDH10. The deletion of the coding region of exon 1 was confirmed by genomic PCR (Fig. 1C). The absence of the PCDH10 protein was confirmed by immunoblotting (Fig. 1D) and immunostaining. Our *Pcdh10* mutant mice were born at the expected Mendelian frequency, developed normally, and were fertile. This is different from the previously reported *Pcdh10*^{LacZ/Neo} KO mice which die prematurely (Uemura et al., 2007), suggesting that the *LacZ/Neo* cassette in the *Pcdh10*^{LacZ/Neo} KO mice had nonspecific effects on their survival.

PCDH10 is dispensable for the growth of striatal and nigrostriatal axons

Because the previously reported *Pcdh10*^{LacZ/Neo} KO mice exhibited impaired striatal axonal growth (Uemura et al., 2007), we first examined the growth of striatal axons in our *Pcdh10* KO (*Pcdh10*^{-/-}) mice. Striatal axons and their terminals were visualized by staining for DARPP-32 (Ouimet and Greengard, 1990). DARPP-32 signal intensities in the striatum and its target regions, the GPe (external globus pallidus), GPi (internal globus pallidus), and SNr (substantia nigra reticulata), were similar between wild-type and *Pcdh10* KO mice, suggesting that striatal axonal growth is normal in the absence of PCDH10 (Fig. 2A; *p* = 0.8724, *t*₍₁₆₎ = 0.1632 for GPe; *p* = 0.9432, *t*₍₁₁₎ = 0.07288 for GPi; *p* = 0.1982, *t*₍₁₆₎ = 1.343 for SNr; *t* test). High-magnification images between the GPi and SNr show that striatal axon fasciculation is also similar between wild-type and *Pcdh10* KO mice (Fig. 2A). We then examined nigrostriatal axonal projections, because the previously reported *Pcdh10*^{LacZ/Neo} KO mice also showed abnormal nigrostriatal axonal projections. TH was used to visualize nigrostriatal axons. TH intensities in the striatum were similar between wild-type and *Pcdh10* KO mice, suggesting that nigrostriatal axonal growth is also normal in the absence of PCDH10 (Fig. 2B; *p* = 0.8993, *t*₍₁₆₎ = 0.1286; *t* test). Furthermore, high-magnification images around the GPe show that dopaminergic axon fasciculation is also similar between wild-type and *Pcdh10* KO mice (Fig. 2B). In addition, we examined overall axonal distributions around the striatum by staining for neurofilament. Our quantification suggests that axonal distributions in the cerebral cortex, striatum, internal capsule, and thalamus are normal in *Pcdh10* KO mice (Fig. 2C; *p* = 0.6660, *t*₍₁₅₎ = 0.4403 for Ctx; *p* = 0.5586, *t*₍₁₅₎ = 0.5982 for Str; *p* = 0.3777, *t*₍₁₅₎ = 0.9091 for int; *p* = 0.5141, *t*₍₁₅₎ = 0.6682 for Th; *t* test). Altogether, our *Pcdh10* KO mice do not show abnormal axonal growth, which contrasts with the previously reported *Pcdh10*^{LacZ/Neo} KO mice (Uemura et al., 2007). Our results indicate that PCDH10 does not play an important role in axon growth.

PCDH10 is localized at synapses in the basolateral nucleus of the amygdala (BLA)

To re-examine the functions of PCDH10, we first investigated the localization of PCDH10 in the brain. Immunostaining for PCDH10 showed that PCDH10 proteins are widely expressed throughout the brain, but its expression levels are particularly

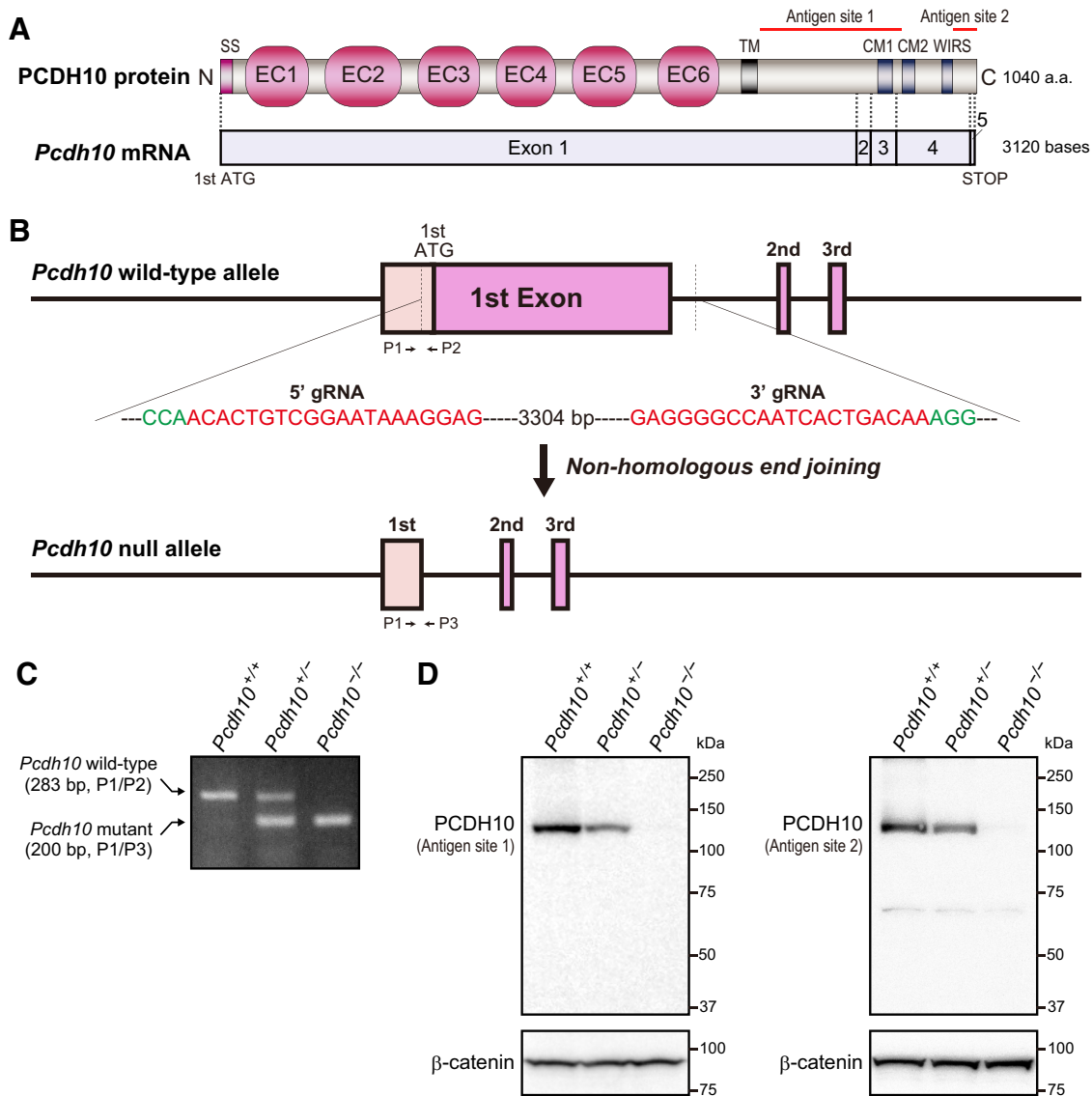


Figure 1. Generation and characterization of a new *Pcdh10* KO mouse line. **A**, Schematic representation of the mouse PCDH10 protein structure (NP_001091641.1; isoform 3) and *Pcdh10* mRNA exons (NM_001098171.1; isoform 3). The antigen sites for our anti-PCDH10 antibodies are indicated in red (Antigen site 1, 728–932 aa; Antigen site 2, 1008–1040 aa). SS, signal sequence; EC, extracellular cadherin domain; TM, transmembrane domain; CM1/2, conserved motifs among the δ -protocadherin family; WIRS, WAVE regulatory complex interacting receptor sequence. **B**, Schematic diagram of the targeting strategy for generating a new *Pcdh10* KO mouse line using the CRISPR/Cas9 system. Two gRNAs (red) are designed to delete the first exon from the *Pcdh10* allele. PAM sequences are in green; P1, P2, and P3, genotyping primers. **C**, Genotyping PCR results with *Pcdh10*^{+/+}, *Pcdh10*^{+/-}, and *Pcdh10*^{-/-} mice. **D**, Immunoblotting with the rabbit anti-PCDH10 antibodies of brain lysates prepared from P10 *Pcdh10*^{+/+}, *Pcdh10*^{+/-}, and *Pcdh10*^{-/-} mice. The two different rabbit anti-PCDH10 antibodies for the Antigen site 1 and 2 both recognize the PCDH10 protein (130 kDa) in *Pcdh10*^{+/+} and *Pcdh10*^{+/-} (about half the amount relative to *Pcdh10*^{+/+}) mice, but not in *Pcdh10*^{-/-} mice. β -Catenin was used as a positive control.

high in the amygdala (Fig. 3A), which is consistent with a previous report (Aoki et al., 2003). In the amygdala, PCDH10 expression was higher in the BLA than lateral amygdala (LA; Fig. 3B). Interestingly, PCDH10 expression was higher in the dorsal BLA than the ventral BLA, showing a gradient expression pattern. This gradient expression pattern was observed both at P10 and P56, suggesting that PCDH10 plays critical roles in the dorsal BLA during development and adulthood. *In situ* hybridization experiments revealed that the expression of *Pcdh10* mRNA is high in the dorsal BLA (Fig. 3C), consistent with the PCDH10 protein localization (Fig. 3B). BLA neurons receive inputs from various regions in the brain, including the BLA itself, LA, prefrontal cortex (PFC), hippocampus, and thalamus (Humeau et al., 2007; Zhang et al., 2021). *Pcdh10* mRNAs were also detected in these brain

regions (Fig. 3C), suggesting that PCDH10 may regulate the connections between these regions and the BLA.

We next examined whether PCDH10 is localized at synapses in the BLA. PFC-BLA, hippocampus-BLA, LA-BLA, and BLA-BLA connections are VGLUT1-positive excitatory synapses; thalamus-BLA connections are VGLUT2-positive excitatory synapses; and inhibitory synapses within the BLA are VGAT positive. Hence, we stained BLA sections for PCDH10, VGLUT1/VGLUT2/VGAT (presynaptic markers), and PSD95/gephyrin (postsynaptic markers for excitatory and inhibitory synapses; Fig. 3D–H). PCDH10 staining showed a punctate pattern in the BLA. PCDH10 co-localized with VGLUT1/PSD95-positive excitatory synapses (Fig. 3E,H; $p < 0.0001$, $t_{(12)} = 12.96$ for VGLUT1/PCDH10; $p < 0.0001$, $t_{(12)} = 12.54$ for PSD95/PCDH10; t test), VGLUT2/PSD95-positive excitatory synapses

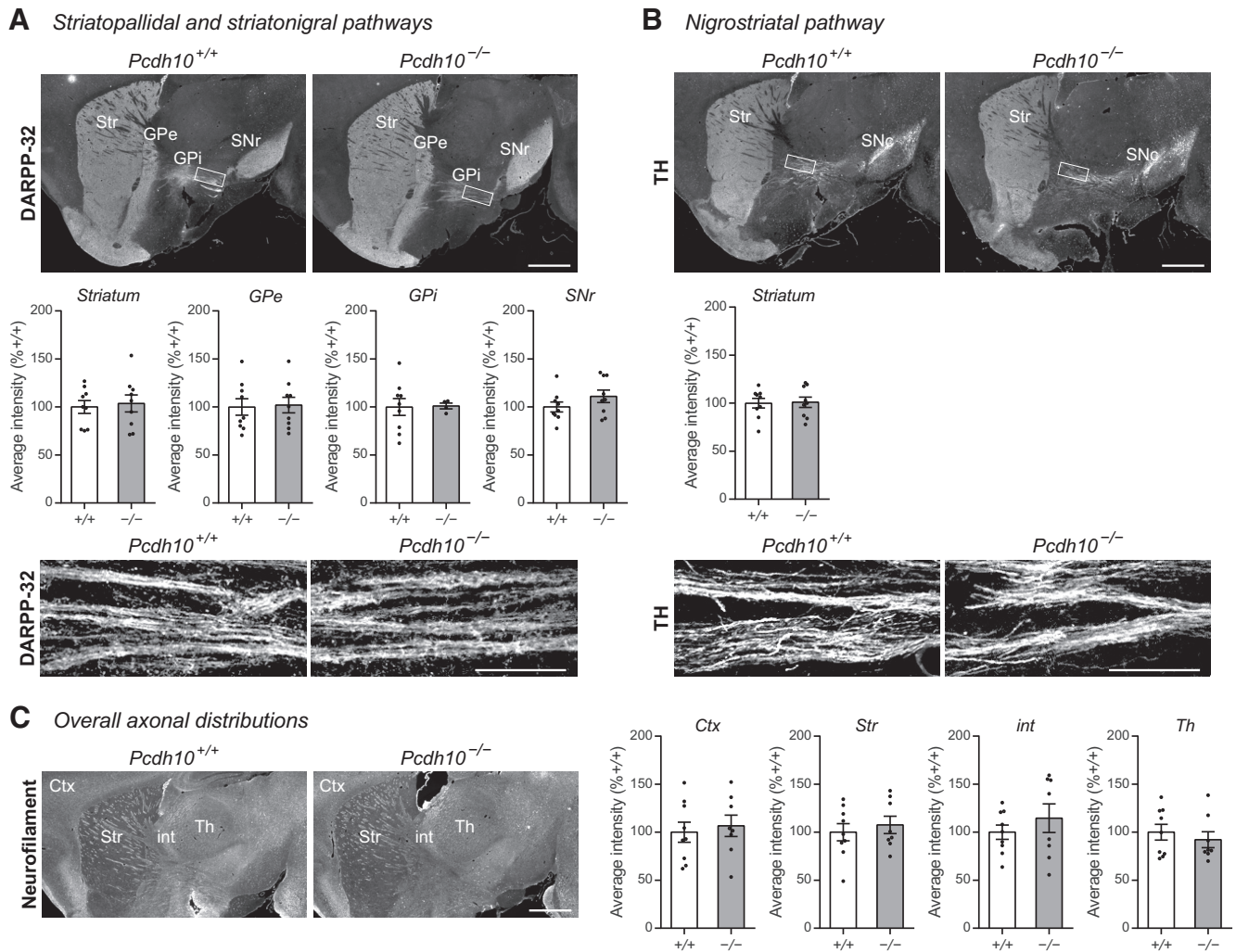


Figure 2. Normal striatal and nigrostriatal axonal projections in *Pcdh10* KO mice. **A**, Immunostaining for DARPP-32 (a marker of striatal neurons) showing normal striatal axonal projections (striatopallidal and striatonigral pathways) in P28 *Pcdh10*^{-/-} mice. Quantification of the staining intensities (%+/+) in the striatum, GPe, GPI, and SNr are shown in the graphs. $n = 4–9$ (total) fields from 3 (total) mice per genotype. High-magnification images of axon bundles, taken from the boxed areas in low-magnification images between GPI and SNr, are shown below. **B**, Immunostaining for TH (a marker of dopaminergic neurons) showing normal nigrostriatal dopaminergic axonal projections in P28 *Pcdh10*^{-/-} mice. Quantification of the staining intensities (%+/+) in the striatum is shown in the graph. $n = 9$ fields from 3 mice per genotype. High-magnification images of axon bundles, taken from the boxed areas in low-magnification images around GPe, are shown below. **C**, Immunostaining for neurofilament (an axonal marker) showing normal overall axonal distributions in *Pcdh10*^{-/-} mice. The mouse anti-neurofilament antibody was used. Quantification of the staining intensities (%+/+) in the cerebral cortex, striatum, internal capsule, and thalamus are shown in the graphs. $n = 8–9$ fields from 3 mice per genotype. The scale bars are 1 mm (**A**, **B**, low magnification, and **C**) and 50 μm (**A**, **B**, high magnification). Data are mean \pm SEM. Student's *t* test (**A–C**). Ctx, cerebral cortex; int, internal capsule; Str, striatum; GPe, globus pallidus external; GPI, globus pallidus internal; SNr, substantia nigra pars reticulata; SNc, substantia nigra pars compacta; Th, thalamus.

(Fig. 3F,H; $p < 0.0001$, $t_{(12)} = 8.897$ for VGLUT2/PCDH10; *t* test), and VGAT/gephyrin-positive inhibitory synapses (Fig. 3G, H; $p < 0.0001$, $t_{(12)} = 11.74$ for VGAT/PCDH10; $p < 0.0001$, $t_{(12)} = 11.91$ for gephyrin/PCDH10; *t* test). These results suggest that PCDH10 is generally localized at synapses, including both excitatory and inhibitory synapses, in the BLA, suggesting that PCDH10 may regulate synapse development, maintenance, and function in the BLA.

Axon projections and dendritic spines are normal in the BLA of *Pcdh10* KO mice

We then evaluated the development of neuronal connections in the BLA in *Pcdh10* KO mice. We first examined axonal projections to the BLA (Fig. 4A). Cortical inputs and thalamic inputs to the BLA were visualized by neurofilament staining as the external capsule (ec) and intermediate capsule (ic), respectively (Fig. 4B). Quantification of staining intensities suggests that these inputs are normal in *Pcdh10* KO mice (Fig. 4B; $p = 0.6029$, $t_{(14)} =$

0.5323 for ec; $p = 0.9678$, $t_{(14)} = 0.04105$ for ic; *t* test). We next used the *Thy1-GFP-M* line, in which GFP is expressed in axon fibers of the hippocampus-BLA projections (Fig. 4C). We found that the number of GFP positive hippocampus-BLA axons ($p = 0.8738$, $t_{(26)} = 0.1604$; *t* test) and the number of axon bundles in the distal hippocampus-BLA projections ($p = 0.6407$, $t_{(26)} = 0.4722$; *t* test) were similar between wild-type and *Pcdh10* KO mice (Fig. 4C). These results indicate that PCDH10 does not play critical roles in the targeting and fasciculation of axon projections to the BLA.

To evaluate the dendrites of BLA neurons in *Pcdh10* KO mice, we first stained the BLA sections for MAP2, a dendritic marker. The intensity of MAP2 in the BLA was similar between wild-type and *Pcdh10* KO mice (Fig. 4D; $p = 0.5388$, $t_{(14)} = 0.6301$; *t* test). To examine dendritic spines, we again used the *Thy1-GFP-M* line. In the *Thy1-GFP-M* line, a small population of BLA pyramidal neurons is labeled with GFP. By mating *Pcdh10* KO mice with the *Thy1-GFP-M* line, we assessed

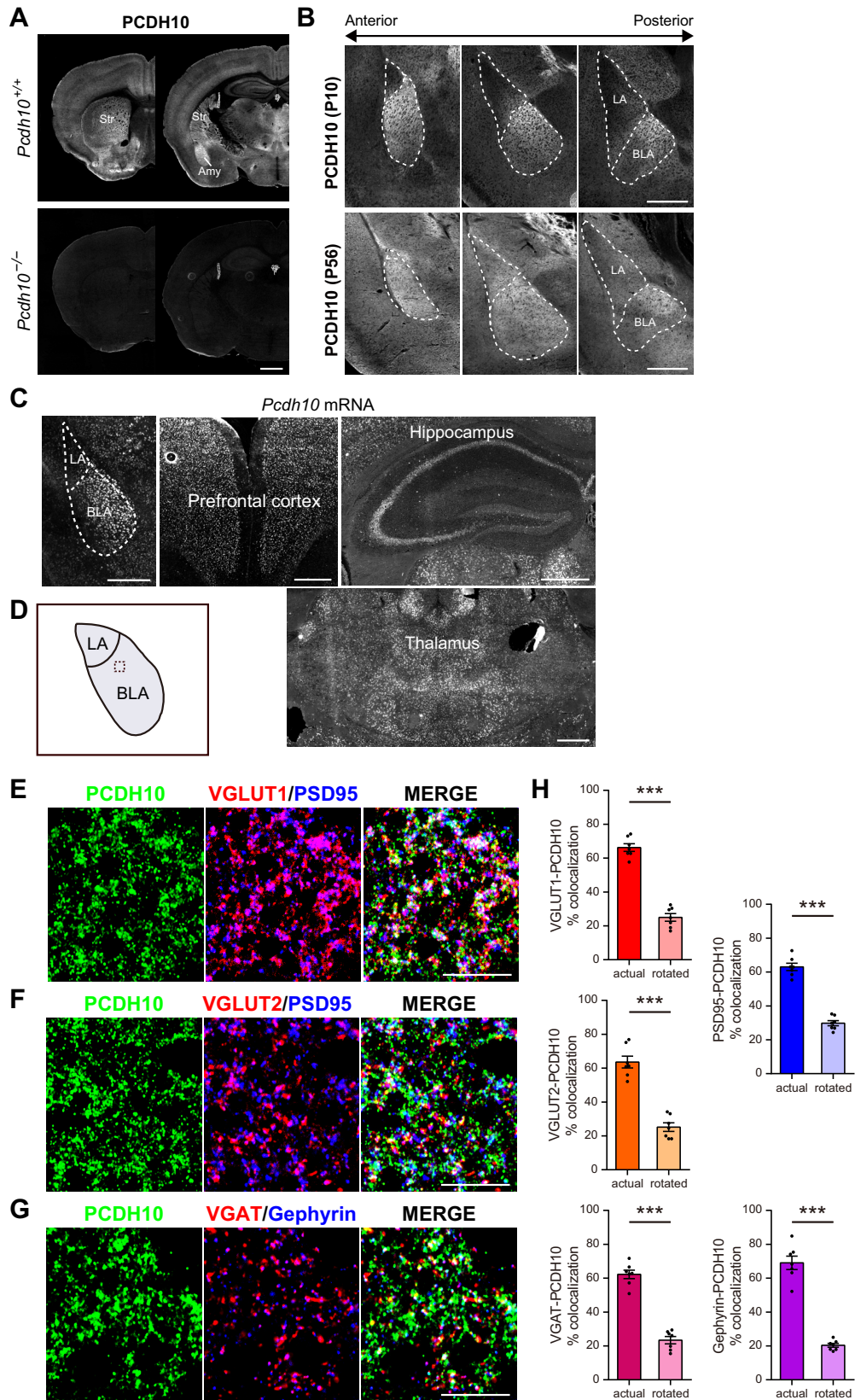


Figure 3. PCDH10 is localized at synapses in the BLA. **A**, Immunostaining with the rabbit anti-PCDH10 antibodies (Antigen site 1) of brain sections from P35 *Pcdh10*^{+/+} and *Pcdh10*^{-/-} mice. PCDH10 is highly expressed in the amygdala. The PCDH10 signal is not detected in *Pcdh10*^{-/-} mice. **B**, Immunostaining with the rat anti-PCDH10 antibodies (Antigen site 1) of amygdala coronal sections along the anterior-posterior axis prepared from P10 and P56 mice. PCDH10 is highly expressed in the dorsal BLA during development and adulthood. **C**, *In situ* hybridization for *Pcdh10* mRNA in the amygdala, PFC, hippocampus, and thalamus of adult mice. **D**, Illustration of the amygdala indicating the pictured area in **E–G**. **E–G**, Triple-staining for PCDH10/VGLUT1/PSD95 (**E**), PCDH10/VGLUT2/PSD95 (**F**), and PCDH10/VGAT/gephyrin (**G**) in the BLA of P28 mice. Rabbit anti-PCDH10 antibodies (Antigen site 1) and the mouse anti-PSD95 (MilliporeSigma) antibody were used in **E**, **F**. Rat anti-PCDH10 antibodies (Antigen site 1) were used in **G**. **H**, Percentages of synaptic-marker puncta colocalized with PCDH10 puncta in the actual and rotated

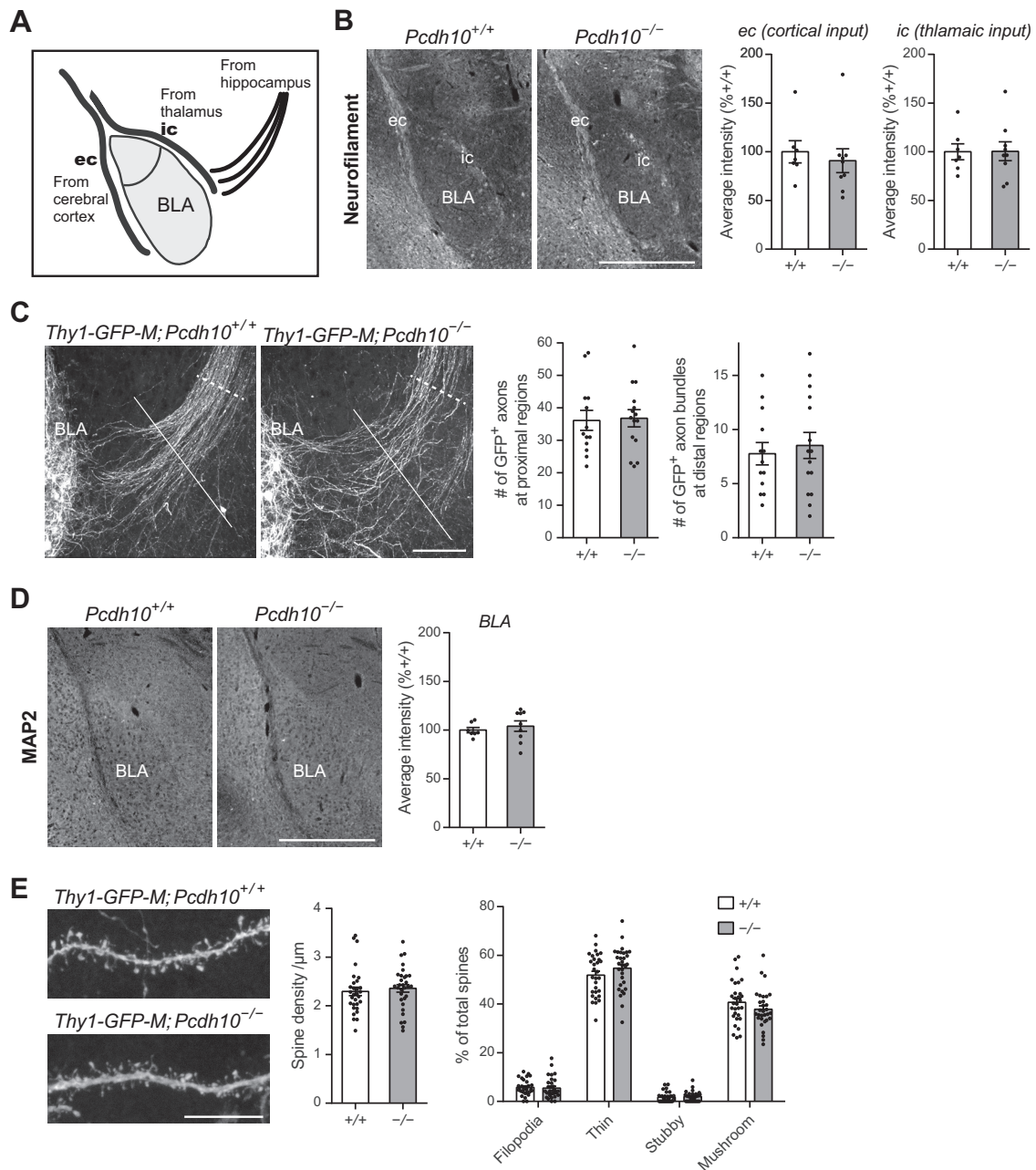


Figure 4. Normal axon projections and dendritic spines in the BLA of *Pcdh10* KO mice. **A**, Illustration indicating the axonal inputs to the BLA examined in **B**, **C**. **B**, Immunostaining for neurofilament showing normal cortical and thalamic input axons to the BLA in P28 *Pcdh10*^{-/-} mice. Rabbit anti-neurofilament antibodies were used. Quantification of the staining intensities (%+/+) in the ec (external capsula: cortical input axons) and ic (internal capsula: thalamic input axons) are shown in the graphs. *n* = 7–9 fields from 3 mice per genotype. **C**, Analysis of the axon fibers of hippocampus-BLA projections in four-week-old *Pcdh10*^{+/+} and *Pcdh10*^{-/-} mice. Hippocampus-BLA projections were visualized by mating *Pcdh10* mice with the *Thy1-GFP-M* line. The number of GFP-labeled hippocampus-BLA axons at proximal regions, quantified at the dotted line, is similar between *Pcdh10*^{+/+} and *Pcdh10*^{-/-} mice. The number of hippocampus-BLA axon bundles at distal regions, quantified at the solid line, is also similar between *Pcdh10*^{+/+} and *Pcdh10*^{-/-} mice. *n* = 13–15 fields from 3–4 mice per genotype. **D**, Immunostaining for MAP2 showing normal dendrite intensities in P28 *Pcdh10*^{-/-} mice. Quantification of the staining intensities (%+/+) in the BLA is shown in the graph. *n* = 7–9 fields from 3 mice per genotype. **E**, Analysis of dendritic spines on BLA neurons in four-week-old *Pcdh10*^{+/+} and *Pcdh10*^{-/-} mice. Dendritic spines were visualized by mating *Pcdh10* mice with the *Thy1-GFP-M* line and classified into filopodia, thin, stubby, and mushroom. The spine density and spine maturation (*n* = 30–31 fields from 3–4 mice per genotype) are similar between *Pcdh10*^{+/+} and *Pcdh10*^{-/-} mice. Data are mean ± SEM. The scale bars are 500 μm (**B**, **D**), 100 μm (**C**), and 10 μm (**E**). Student's *t* test (**B–E**).

dendritic spine development in the BLA. We found that the density and maturation of dendritic spines are not significantly

different between wild-type and *Pcdh10* KO mice (Fig. 4E; *p* = 0.5994, *t*₍₅₉₎ = 0.5281 for spine density; *p* > 0.05 for each spine classification; *t* test). These results suggest that PCDH10 does not regulate dendrite and spine development in the BLA.

Synaptic defects in the BLA of *Pcdh10* KO mice

We next investigated synapse development in the BLA of *Pcdh10* KO mice. Because PCDH10 is localized at VGLUT1-positive and

←

images. *n* = 7 fields from 3–4 WT mice for actual and rotated images (**E–G**). The scale bars are 1 mm (**A**), 0.5 mm (**B**, **C**), and 10 μm (**E–G**). Data are mean ± SEM; ****p* < 0.005; Student's *t* test (**H**). Str, striatum; Amy, amygdala; LA, lateral amygdala; BLA, basolateral nucleus of the amygdala.

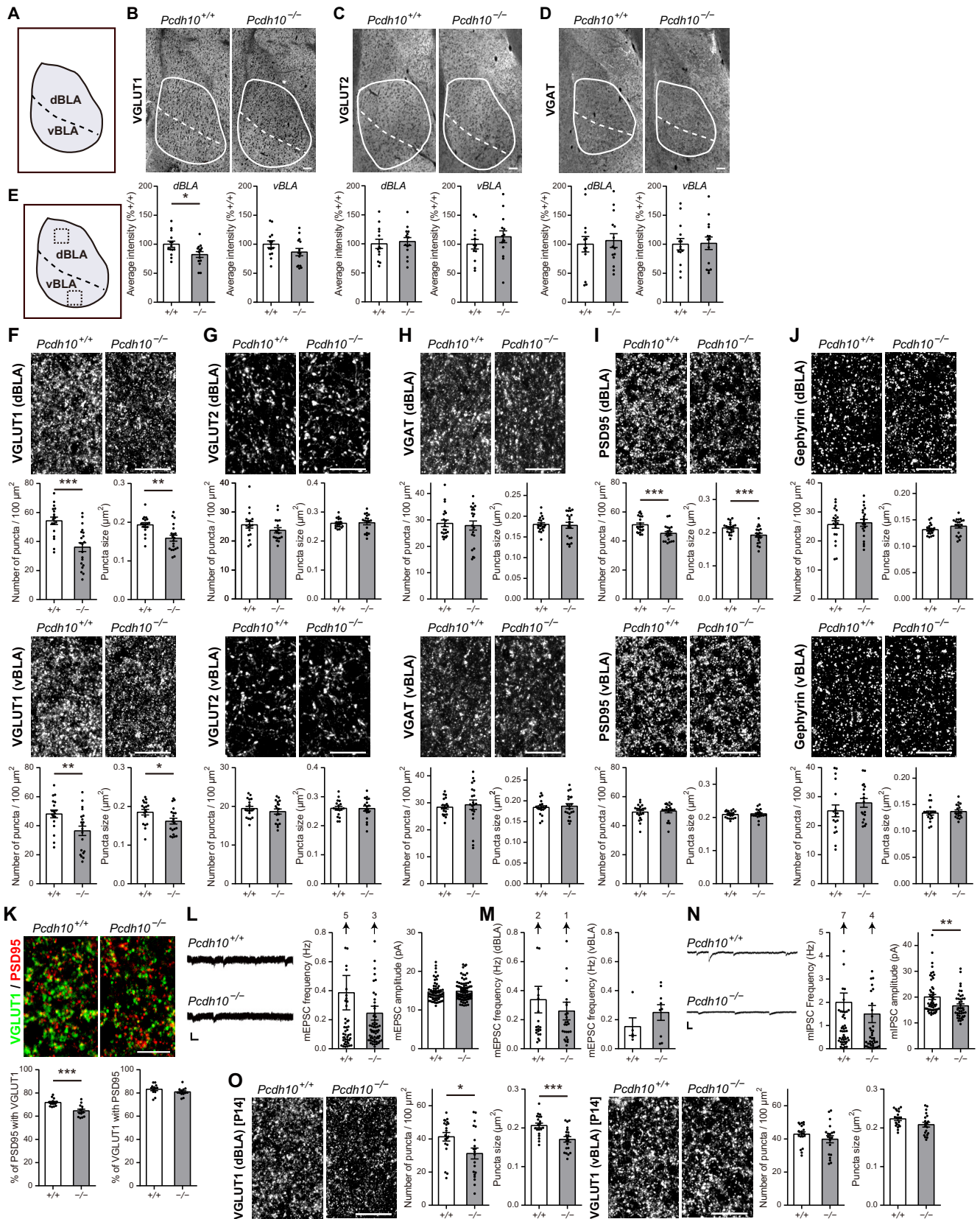


Figure 5. *Pcdh10* KO mice exhibit synaptic defects in the BLA. **A**, Illustration indicating the dorsal BLA (dBLA) and ventral BLA (vBLA) examined in **B–D**. **B–D**, Immunostaining for VGLUT1 (**B**), VGLUT2 (**C**), or VGAT (**D**) in the amygdala of four-week-old *Pcdh10*^{+/+} and *Pcdh10*^{-/-} mice. Quantification of the staining intensities (%+/+) in the dorsal BLA and ventral BLA are shown in the graphs. The intensity of VGLUT1 puncta is significantly decreased in the dorsal BLA in *Pcdh10*^{-/-} mice relative to *Pcdh10*^{+/+} mice. The intensities of VGLUT2 and VGAT puncta in the BLA are similar between *Pcdh10*^{+/+} and *Pcdh10*^{-/-} mice. *n* = 14 fields from 5 mice per genotype for VGLUT1 (**B**). *n* = 13–14 fields from 7 mice per genotype for VGLUT2 (**C**). *n* = 14 fields from 6 mice per genotype for VGAT (**D**). **E**, Illustration indicating the pictured area in **F–J**. **F–J**, Immunostaining for VGLUT1 (**F**), VGLUT2 (**G**), VGAT (**H**), PSD95 (**I**), or gephyrin (**J**) in the dorsal BLA and ventral BLA of P28 *Pcdh10*^{+/+} and *Pcdh10*^{-/-} mice. The mouse anti-PSD95 (NeuroMab) antibody was used. The density and size of VGLUT1 puncta in the dorsal BLA and ventral

VGLUT2-positive excitatory synapses as well as VGAT-positive inhibitory synapses (Fig. 3), we examined these three types of synapses in the BLA at P28, at the end of synapse development. To evaluate presynaptic development, we quantified VGLUT1-positive, VGLUT2-positive, and VGAT-positive puncta in the BLA. The intensities of VGLUT1 puncta were significantly decreased in the dorsal BLA in *Pcdh10* KO mice compared with wild-type mice (Fig. 5A,B; $p = 0.0230$, $t_{(26)} = 2.417$; t test). There also seems to be a decrease in the intensity of VGLUT1 puncta in the ventral BLA in *Pcdh10* KO mice, but the decrease was not significant ($p = 0.1321$, $t_{(26)} = 1.555$; t test). These results are consistent with the relatively higher expression levels of PCDH10 in the dorsal BLA than ventral BLA (Fig. 3B). The intensities of VGLUT2-positive and VGAT-positive puncta in the BLA were not significantly different between wild-type and *Pcdh10* KO mice in both the dorsal and ventral BLA (Fig. 5C,D; $p > 0.05$ for VGAT and VGLUT2 intensities; t test). We also examined the densities and sizes of puncta for VGLUT1, VGLUT2, and VGAT in the dorsal and ventral BLA at P28 (Fig. 5E–H). Although the average intensity for VGLUT1 was significantly decreased only in the dorsal BLA (Fig. 5B), we found that the density and size of VGLUT1 puncta were decreased both in the dorsal BLA and ventral BLA of *Pcdh10* KO mice at P28 (Fig. 5F; $p < 0.0001$, $t_{(36)} = 4.509$, density in dorsal BLA; $p = 0.0010$, $t_{(36)} = 3.573$, size in dorsal BLA; $p = 0.0096$, $t_{(36)} = 2.735$, density in ventral BLA; $p = 0.0318$, $t_{(36)} = 2.234$, size in ventral BLA; t test). The decrease was more robust in the dorsal BLA than ventral BLA in *Pcdh10* KO mice. VGLUT2 and VGAT puncta were not significantly different by any measured criteria between wild-type and *Pcdh10* KO mice (Fig. 5G,H; $p > 0.05$; t test). These results suggest that PCDH10 primarily regulates the development of VGLUT1-positive, but not VGLUT2-positive or VGAT-positive, presynaptic terminals in the BLA.

←

BLA are decreased in *Pcdh10*^{-/-} mice relative to *Pcdh10*^{+/+} mice (F). The density and size of PSD95 puncta in the dorsal BLA, but not the ventral BLA, are decreased in *Pcdh10*^{-/-} mice relative to *Pcdh10*^{+/+} mice (I). The density and size of VGAT (H), VGLUT2 (G), and gephyrin (J) in the dorsal BLA and ventral BLA are similar between *Pcdh10*^{+/+} and *Pcdh10*^{-/-} mice. $n = 18$ –20 fields from 5 mice per genotype for VGLUT1 in the dorsal and ventral BLA (F). $n = 18$ fields from 4 mice per genotype for VGLUT2 in the dorsal and ventral BLA (G). $n = 20$ fields from 3–4 mice per genotype for PSD95 in the dorsal and ventral BLA (H). $n = 18$ –20 fields from 3 mice per genotype for gephyrin in the dorsal and ventral BLA (J). $n = 20$ fields from 4 mice per genotype for VGAT in the dorsal and ventral BLA (I). K, Double-staining for VGLUT1/PSD95 in the dorsal BLA of P28 mice. Percentage of PSD95 colocalized with VGLUT1 puncta (% PSD95 with VGLUT1), but not that of VGLUT1 colocalized with PSD95 puncta (% VGLUT1 with PSD95), is decreased in *Pcdh10*^{-/-} mice relative to in *Pcdh10*^{+/+} mice. $n = 13$ fields from 4 mice per genotype. L, mEPSCs recorded from BLA neurons (entire BLA, with more cells located in the dorsal than ventral BLA) of four- to five-week-old *Pcdh10*^{+/+} and *Pcdh10*^{-/-} mice. The frequency of mEPSC appears decreased in *Pcdh10*^{-/-} mice relative to in *Pcdh10*^{+/+} mice. $n = 49$ cells for *Pcdh10*^{+/+} and 61 cells for *Pcdh10*^{-/-} from 4 mice, respectively. M, mEPSCs recorded from dorsal and ventral BLA neurons of four- to five-week-old *Pcdh10*^{+/+} and *Pcdh10*^{-/-} mice. $n = 22$ cells for *Pcdh10*^{+/+} and 26 cells for *Pcdh10*^{-/-} from 4 mice in dorsal BLA. $n = 5$ cells for *Pcdh10*^{+/+} and 9 cells for *Pcdh10*^{-/-} from 4 mice in ventral BLA. N, mIPSCs recorded from dorsal BLA neurons of four- to five-week-old *Pcdh10*^{+/+} and *Pcdh10*^{-/-} mice. The amplitude of mIPSC is decreased in *Pcdh10*^{-/-} mice relative to in *Pcdh10*^{+/+} mice. $n = 51$ cells for *Pcdh10*^{+/+} and 42 cells for *Pcdh10*^{-/-} from 4 mice, respectively. O, Immunostaining for VGLUT1 in the dorsal BLA and ventral BLA of P14 *Pcdh10*^{+/+} and *Pcdh10*^{-/-} mice. The density and size of VGLUT1 puncta in the dorsal BLA, but not in the ventral BLA, are decreased in *Pcdh10*^{-/-} mice relative to *Pcdh10*^{+/+} mice. The scale bars are 100 μ m (B–D), 10 μ m (F–J, O), 5 μ m (K), 10 pA and 25 ms (L), and 50 pA and 25 ms (M). Data are mean \pm SEM. Arrows and number in the graphs indicate the number of data points greater than the maximum value of the y-axis (L–N). * $p < 0.05$, ** $p < 0.01$, *** $p < 0.005$; Student's t test.

To evaluate postsynaptic development, we performed staining for PSD95 and gephyrin in the dorsal and ventral BLA at P28 (Fig. 5E,I). We found that the density and size of PSD95 puncta were significantly decreased in the dorsal BLA, but not in the ventral BLA of *Pcdh10* KO mice (Fig. 5I; $p = 0.0017$, $t_{(38)} = 3.370$, density in dorsal BLA; $p = 0.0028$, $t_{(38)} = 3.197$, size in dorsal BLA; $p = 0.6483$, $t_{(38)} = 0.4598$, density in ventral BLA; $p = 0.6215$, $t_{(38)} = 0.4978$, size in ventral BLA; t test). The density and size of gephyrin puncta were similar between wild-type and *Pcdh10* KO mice (Fig. 5J; $p = 0.7428$, $t_{(38)} = 0.3306$, density in dorsal BLA; $p = 0.1271$, $t_{(38)} = 1.560$, size in dorsal BLA; $p = 0.2840$, $t_{(34)} = 1.089$, density in ventral BLA; $p = 0.5472$, $t_{(34)} = 0.6081$, size in ventral BLA; t test). These results suggest that postsynaptic development of excitatory synapses, but not inhibitory synapses, is impaired in the BLA of *Pcdh10* KO mice.

We also examined the colocalization of VGLUT1 and PSD95 puncta in the dorsal BLA of wild-type and *Pcdh10* KO mice. We found that the percentage of PSD95 colocalized with VGLUT1 was significantly decreased in *Pcdh10* KO mice (Fig. 5K; $p = 0.0003$, $t_{(24)} = 4.234$). Altogether, our results suggest that PCDH10 regulates synaptic development of VGLUT1-positive excitatory synapses in the BLA.

To further characterize the synaptic defects in *Pcdh10* KO mice, we performed electrophysiological analysis of synapses in the BLA at P28. We recorded mEPSCs from BLA neurons (entire BLA, with more cells located in the dorsal than ventral BLA). The frequency of mEPSCs appeared reduced in *Pcdh10* KO mice ($p = 0.2335$, $t_{(106)} = 1.198$; t test), while the amplitude of mEPSC was not changed in *Pcdh10* KO mice ($p = 0.6120$, $t_{(149)} = 0.5082$; t test; Fig. 5L). We then recorded and compared the frequency of mEPSCs in dorsal BLA and ventral BLA neurons. Although not statistically significant, the mEPSC frequency seems to be decreased in the dorsal BLA, but not in the ventral BLA (Fig. 5M; $p = 0.4638$ and 0.2770 , respectively; t test). These results suggest that the presynaptic function of excitatory synapses is impaired in *Pcdh10* KO mice. We also recorded mIPSCs from dorsal BLA neurons in wild-type and *Pcdh10* KO mice. We found that, while immunostaining for inhibitory synaptic markers (VGAT and gephyrin) did not show any changes, the amplitude of mIPSCs is significantly decreased in *Pcdh10* KO neurons (Fig. 5N; $p = 0.0083$, $t_{(91)} = 2.699$; t test). These results may suggest that changes at excitatory synapses are influencing inhibitory synaptic function.

Because immunostaining for VGLUT1 at P28 showed that the density and size of VGLUT1 puncta are decreased both in the dorsal and ventral BLA in *Pcdh10* KO mice relative to wild-type mice (Fig. 5F), we examined VGLUT1 puncta earlier, at P14, during synapse formation. We found that the density and size of VGLUT1 puncta are significantly decreased in the dorsal BLA, but not in the ventral BLA, in *Pcdh10* KO mice relative to wild-type mice (Fig. 5O; $p = 0.0208$, $t_{(38)} = 2.411$, density in dorsal BLA; $p = 0.0004$, $t_{(38)} = 3.906$, size in dorsal BLA; $p = 0.2423$, $t_{(38)} = 1.188$, density in ventral BLA; $p = 0.0569$, $t_{(38)} = 1.964$, size in ventral BLA; t test). These results suggest that during synapse formation (P14), PCDH10 primarily organizes synapses in the dorsal BLA, but not in the ventral BLA. Defects in synapse development in the dorsal BLA (at P14) may contribute to subsequent changes in the ventral BLA synapses (at P28).

Reduced anxiety-related behaviors in *Pcdh10* KO mice

Synapses in the dorsal BLA controls negative emotional behaviors such as anxiety-related behaviors (Beyeler et al., 2018) and fear-related behaviors (Kim et al., 2016). Because *Pcdh10* KO

mice showed synaptic defects in the dorsal BLA, we performed a battery of behavioral tests examining anxiety, fear, and mood, which are also relevant to ASD and co-occurring conditions. We used two- to four-month-old male mice for the behavioral tests (Figs. 6–8) except for the USV test in which pups were used (Fig. 7C).

We first examined anxiety-related behaviors. In the elevated plus maze, increases in anxiety-like behaviors manifest as more time spent in the closed arms than in the open arms. Compared with wild-type mice, *Pcdh10* KO mice spent significantly more time in the open arms ($p = 0.0009$, $t_{(23)} = 3.811$; t test) and less time in the closed arms ($p = 0.0144$, $t_{(23)} = 2.648$; t test), suggesting that *Pcdh10* KO mice display reduced anxiety-like behaviors (Fig. 6A). We then performed the light/dark transition test to further evaluate anxiety levels. In this test, the motivation to explore novel areas conflicts with the desire to avoid higher light conditions. *Pcdh10* KO mice explored the light area for significantly more time than wild-type mice (Fig. 6B; $p = 0.0033$, $t_{(23)} = 3.275$; t test). In addition, the transition number was significantly higher in *Pcdh10* KO mice than wild-type mice (Fig. 6B; $p = 0.0032$, $t_{(23)} = 3.285$; t test), indicating that *Pcdh10* KO mice explored the light area more frequently. These results are consistent with the notion that *Pcdh10* KO mice show reduced anxiety-like behaviors.

To exclude the possibility that the changes in the anxiety tests are because of defects in visual function in *Pcdh10* KO mice, we performed a visual test using touch screen operant chambers, which requires touching a panel in response to visual stimuli. We found no difference in this test between wild-type and *Pcdh10* KO mice (Fig. 6C; $p = 0.8563$, $t_{(21)} = 0.1833$; t test), suggesting that the vision of *Pcdh10* KO mice is normal. Altogether, these results indicate that anxiety levels are reduced in *Pcdh10* KO mice.

Impaired fear conditioning in *Pcdh10* KO mice

We next examined fear-related behaviors. For this, we conducted contextual and cued fear conditioning tests. On day 1, mice received a foot shock associated with a conditioned tone three times in a contextual chamber (conditioning session). On day 2, mice were returned to the same contextual chamber, and freezing responses were monitored (contextual test). On day 3, mice were put in a different contextual chamber, then the conditioned tone was presented, and freezing responses were monitored (cued test). On the conditioning day, *Pcdh10* KO mice showed significantly decreased freezing responses relative to wild-type mice as they receive foot shocks (Fig. 6D; $p = 0.0010$, $F_{(1,23)} = 14.10$; two-way repeated-measures ANOVA). *Pcdh10* KO mice also showed decreased freezing levels both in the contextual test and cued test compared with wild-type mice (Fig. 6D; $p = 0.0005$, $F_{(1,23)} = 16.38$, contextual test; $p = 0.0001$, $F_{(1,23)} = 20.89$, cued test; two-way repeated-measures ANOVA); however, the *Pcdh10* KO mice did show freezing responses to the level that they were conditioned on day 1. These results suggest that *Pcdh10* KO mice exhibit impaired fear acquisition, but have relatively normal fear memory.

To exclude the possibility that decreased pain sensitivity in *Pcdh10* KO mice underlies their defects in fear conditioning, we performed a hot plate test to assess their sensitivity to a painful stimulus. We found no significant difference in the withdrawal latency between wild-type and *Pcdh10* KO mice (Fig. 6E; $p = 0.0638$, $t_{(23)} = 1.947$; t test), suggesting that the pain sensitivity of *Pcdh10* mice is normal.

We also examined the phenotype of *Pcdh10* heterozygous (*Pcdh10*^{+/-}) mice by performing the fear conditioning test. We found that during conditioning, *Pcdh10*^{+/-} mice showed a slightly reduced freezing response, between the second and third foot shocks, compared with wild-type mice (Fig. 6F; $p < 0.0100$, for 5–6 min, two-way repeated-measures ANOVA followed by the Sidak's test). The freezing response after the third foot shock was comparable between wild-type and *Pcdh10*^{+/-} mice. Freezing responses during the context and cued tests were not different between wild-type and *Pcdh10*^{+/-} mice (Fig. 6F; $p = 0.3834$, $F_{(1,9)} = 0.8396$, contextual test; $p = 0.6963$, $F_{(1,9)} = 0.1624$; cued test; two-way repeated-measures ANOVA). These results suggest that *Pcdh10*^{+/-} mice show a mild impairment in fear acquisition.

Decreased stress-coping responses in *Pcdh10* KO mice

To assess the stress-coping style of *Pcdh10* KO mice, we tested the mice with the tail suspension test and the forced swim test. In these tests, increased immobility during the tests is correlated with an increase in passive stress-coping behaviors. In the tail suspension test, *Pcdh10* KO mice were significantly less immobile than wild-type mice [$p = 0.0116$, $F_{(1,23)} = 7.521$, two-way repeated-measures ANOVA (Fig. 6G, left); $p = 0.0116$, $t_{(23)} = 2.742$, t test (Fig. 6G, right)]. However, in the forced swim test, wild-type and *Pcdh10* KO mice showed a similar amount of immobility time [$p = 0.9669$, $F_{(1,23)} = 0.001758$, two-way repeated-measures ANOVA (Fig. 6H, left); $p = 0.9669$, $t_{(23)} = 0.04193$, t test (Fig. 6H, right)]. In the tail suspension and forced swim test, immobility is induced by different types of stress. For example, tail suspension involves hemodynamic stress (Cryan et al., 2005). Our results suggest that *Pcdh10* KO mice exhibit decreased passive coping with certain types of stress, such as tail suspension.

Reduced social recognition and social communication in *Pcdh10* KO mice

We then asked whether *Pcdh10* KO mice show ASD-like behaviors, such as impaired social interaction and recognition, altered social communication, and repetitive behaviors. We first performed the three-chamber social interaction test to examine the sociability of mice. For this, we examined whether mice display a preference for a stranger mouse (S) to an empty (E) cage. We found that both wild-type and *Pcdh10* KO mice spent more time around a stranger cage than an empty cage (Fig. 7A; $p < 0.0001$, $t_{(22)} = 6.340$, wild-type; $p < 0.0001$, $t_{(22)} = 9.118$, KO; t test). The preference index was similar between wild-type and *Pcdh10* KO mice, suggesting that social interaction is normal in *Pcdh10* KO mice (Fig. 7A; $p = 0.5448$, $t_{(22)} = 0.6152$; t test). After the social interaction test, a novel mouse (N) was introduced into the previously empty cage. In this social recognition test, the stranger mouse (S) in the social interaction test would now become the familiar mouse (F). We found that both wild-type and *Pcdh10* KO mice spent more time around the novel mouse than the familiar mouse (Fig. 7A; $p = 0.0001$, $t_{(22)} = 4.672$, wild-type; $p = 0.0100$, $t_{(22)} = 2.820$, KO; t test). However, the preference index appears to be decreased in *Pcdh10* KO mice relative to wild-type mice (Fig. 7A; $p = 0.0516$, $t_{(22)} = 2.058$; t test). These results suggest that *Pcdh10* KO mice may display normal social interaction, but reduced social recognition.

We next examined repetitive behaviors by monitoring grooming and rearing. The grooming duration ($p = 0.7424$, $t_{(23)} = 0.3326$; t test) and rearing number ($p = 0.7492$, $t_{(23)} = 0.3235$; t test) were similar between wild-type and *Pcdh10* KO

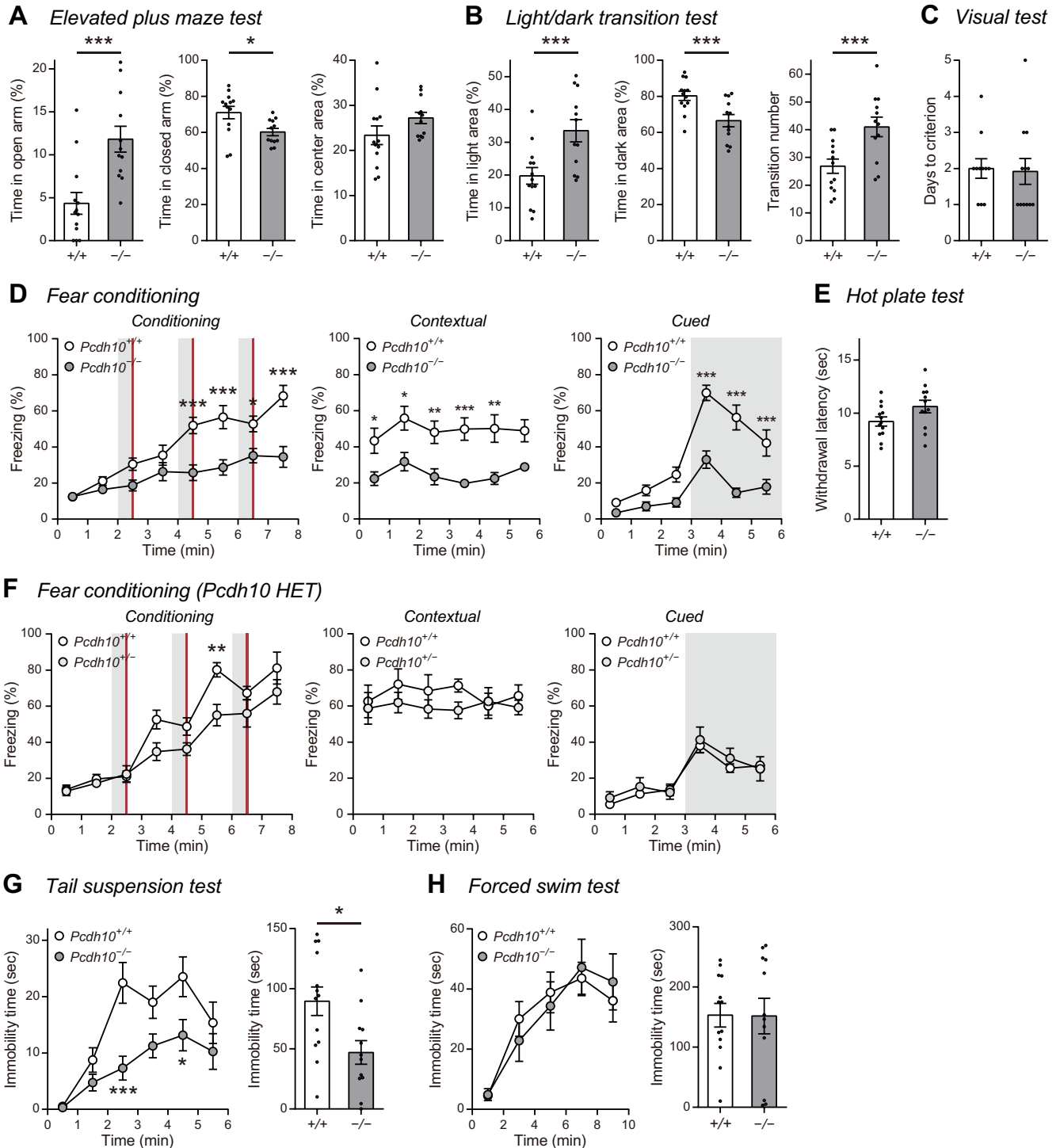


Figure 6. *Pcdh10* KO mice show anxiety-related behaviors, impaired fear conditioning, and decreased stress-coping responses. **A**, Elevated plus maze test. Times spent in the open arm and the closed arm are increased and decreased, respectively, in *Pcdh10*^{-/-} mice relative to *Pcdh10*^{+/+} mice. *n* = 13 mice for *Pcdh10*^{+/+} and 12 for *Pcdh10*^{-/-}. **B**, Light/dark transition test. Times spent in the light area and the dark area are increased and decreased, respectively, in *Pcdh10*^{-/-} mice relative to *Pcdh10*^{+/+} mice. *n* = 13 mice for *Pcdh10*^{+/+} and 12 for *Pcdh10*^{-/-}. **C**, Visual test. Days required to the criterion are similar between *Pcdh10*^{+/+} and *Pcdh10*^{-/-} mice. *n* = 11 mice for *Pcdh10*^{+/+} and 12 for *Pcdh10*^{-/-}. **D, F**, Fear conditioning test with *Pcdh10*^{+/+} and *Pcdh10*^{-/-} mice (**D**) or with *Pcdh10*^{+/+} and *Pcdh10*^{+/-} mice (**F**). Left, Freezing responses during conditioning on day 1. CS is presented for 30 s, three times (gray shadows). At the end of each CS, a US was given (red). CS, 10-kHz tone; US, 0.3-mA foot shock. Middle, Freezing responses during the contextual test on day 2. Right, Freezing responses during the cued test on day 3. CS is presented at 3–6 min (gray shadow). Freezing responses during the conditioning, contextual, and cued tests are reduced in *Pcdh10*^{-/-} mice relative to *Pcdh10*^{+/+} mice (**D**). *n* = 13 mice for *Pcdh10*^{+/+} and 12 for *Pcdh10*^{-/-}. Freezing responses between the second and third foot shocks during the conditioning are slightly reduced in *Pcdh10*^{+/-} mice relative to *Pcdh10*^{+/+} mice (**F**). *n* = 5 mice for *Pcdh10*^{+/+} and 6 for *Pcdh10*^{+/-}. **E**, Hot plate test. The withdrawal latency is similar between *Pcdh10*^{+/+} and *Pcdh10*^{-/-} mice. *n* = 13 mice for *Pcdh10*^{+/+} and 12 for *Pcdh10*^{-/-}. **G**, Tail suspension test. Left, Immobility time is measured for 6 min. Right, Cumulative immobility time during the 6-min test session. Immobility time is reduced in *Pcdh10*^{-/-} mice relative to *Pcdh10*^{+/+} mice. *n* = 13 mice for *Pcdh10*^{+/+} and 12 for *Pcdh10*^{-/-}. **H**, Forced swim test. Left, Immobility time is measured for 10 min. Right, Cumulative immobility time during the 10-min test session. Immobility time is similar between *Pcdh10*^{+/+} and *Pcdh10*^{-/-} mice. *n* = 13 mice for *Pcdh10*^{+/+} and 12 for *Pcdh10*^{-/-}. Data are mean ± SEM. **p* < 0.05, ***p* < 0.01, ****p* < 0.005; Student's *t* test (**A–C**, **E**, **G**, right, **H**, right). **p* < 0.05, ***p* < 0.01, ****p* < 0.005; two-way repeated-measures ANOVA followed by the Sidak's test (**D**, **F**, **G**, left, **H**, left).

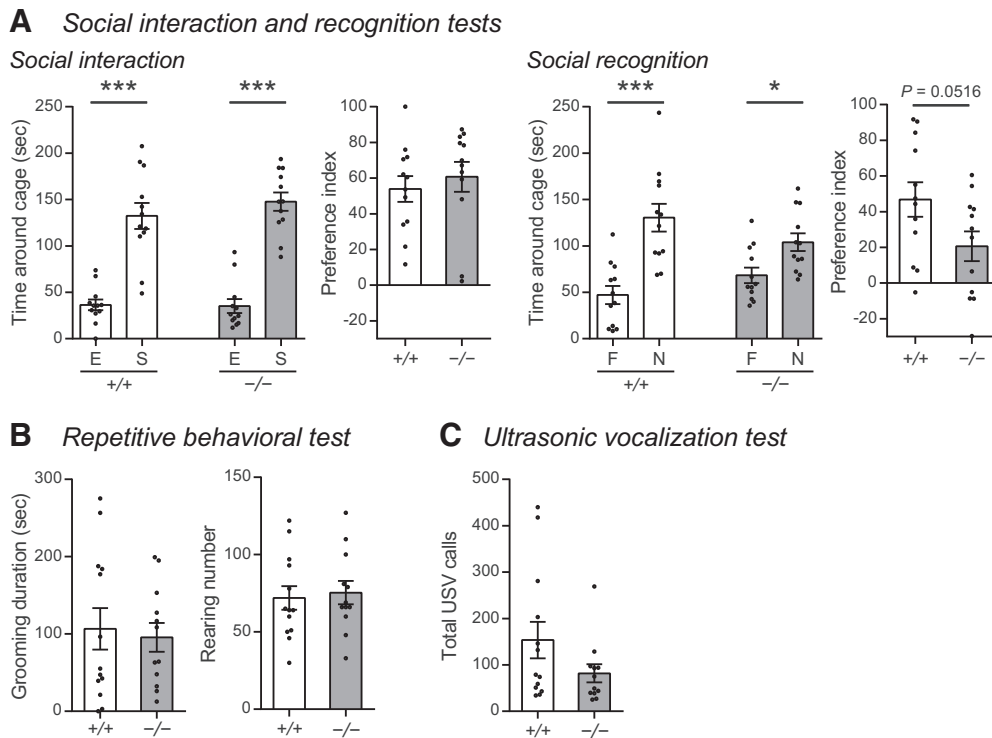


Figure 7. *Pcdh10* KO mice show reduced social recognition and social communication. **A**, Social interaction and recognition tests. Left, Social interaction test. Both *Pcdh10*^{+/+} and *Pcdh10*^{-/-} mice spend significantly more time around the cage containing a stranger mouse (S) than the empty cage (E). Preference index [(S – E)/(S + E) × 100] is similar between *Pcdh10*^{+/+} and *Pcdh10*^{-/-} mice. Right, Social recognition test. Both *Pcdh10*^{+/+} and *Pcdh10*^{-/-} mice spend significantly more time around the cage containing a novel mouse (N) than the cage containing a familiar mouse (F). However, the preference index [(N – F)/(N + F) × 100] is reduced in *Pcdh10*^{-/-} mice relative to *Pcdh10*^{+/+} mice ($p = 0.0516$). $n = 12$ mice for *Pcdh10*^{+/+} and 12 for *Pcdh10*^{-/-}. **B**, Repetitive behavioral test. Grooming duration and rearing number are similar between *Pcdh10*^{+/+} and *Pcdh10*^{-/-} mice. $n = 13$ mice for *Pcdh10*^{+/+} and 12 for *Pcdh10*^{-/-}. **C**, USV test. The number of total USV calls is reduced in *Pcdh10*^{-/-} mice relative to *Pcdh10*^{+/+} mice. $n = 13$ mice for *Pcdh10*^{+/+} and 12 for *Pcdh10*^{-/-} mice. Data are mean ± SEM; * $p < 0.05$, *** $p < 0.005$; Student's t test (**A–C**).

mice, suggesting that *Pcdh10* KO mice do not show abnormal repetitive behaviors (Fig. 7B).

We then performed the USV test to evaluate social communication. P6 to P8 male pups were separated from their mother and placed alone in a USV chamber, and total USV calls were recorded. We found that the total USV calls appear to be decreased in *Pcdh10* KO mice relative to wild-type mice (Fig. 7C; $p = 0.1258$, $t_{(23)} = 1.586$; t test). These results suggest that *Pcdh10* KO mice may show reduced social communication.

Normal sensory and motor behaviors in *Pcdh10* KO mice

Finally, we examined whether sensory and motor functions are altered in *Pcdh10* KO mice. For this, we first performed the open field test to examine spontaneous locomotor activity. We monitored the distance traveled in the open field box. The distance traveled was not significantly different between wild-type and *Pcdh10* KO mice (Fig. 8A; $p = 0.1405$, $t_{(23)} = 1.527$; t test), suggesting that spontaneous locomotor activity is normal in *Pcdh10* KO mice. We next conducted the accelerating rotarod test to examine motor learning. The retention time on the accelerating rotarod across six trials was similar between wild-type and *Pcdh10* KO mice (Fig. 8B; $p > 0.05$ for each trial; t test), suggesting that motor learning ability is normal in *Pcdh10* KO mice.

We then performed ASR and PPI tests to examine sensorimotor information processing in *Pcdh10* KO mice. In the ASR test, startle responses were similar between wild-type and *Pcdh10* KO mice (Fig. 8C; $p > 0.05$ for each startle stimulus; t test). In the PPI test, *Pcdh10* KO mice exhibited similar levels of PPI

compared with wild-type mice (Fig. 8D; $p > 0.05$ for each pre-pulse level; t test). These results suggest that startle response to sensory stimulation and sensorimotor gating ability are normal in *Pcdh10* KO mice. Altogether, *Pcdh10* KO mice have normal sensory and motor functions.

Discussion

In this study, we established a new *Pcdh10* mutant mouse line using the CRISPR/Cas9 system and revealed that PCDH10 plays critical roles in excitatory synapse development in the dorsal BLA and regulates anxiety-related, fear-related, and stress-related behaviors.

Pcdh10 KO mice show synaptic defects but not axonal defects: possible nonspecific effects of the *LacZ/Neo* cassette

A previously published paper reported that their *Pcdh10* mutant (*Pcdh10*^{LacZ/Neo} KO) mice showed altered axonal projections in embryonic or early postnatal stages and were postnatally lethal (Uemura et al., 2007). In contrast, our newly generated *Pcdh10* KO mice did not show axonal defects at P28 (Fig. 2) and were healthy and fertile. We postulate that some of the phenotypes in *Pcdh10*^{LacZ/Neo} KO mice might have been because of the *LacZ/Neo* cassette inserted in the mouse line. It is known that the insertion of a *Neo* cassette could interfere with the expression of the target gene and surrounding genes (Pham et al., 1996; Müller, 1999). In addition, β -galactosidase expression from the *LacZ* gene may cause cellular toxicity (Kimura et al., 1994; Detrait et al., 2002; Krestel et al., 2004). Indeed, a *Pcdh17* KO

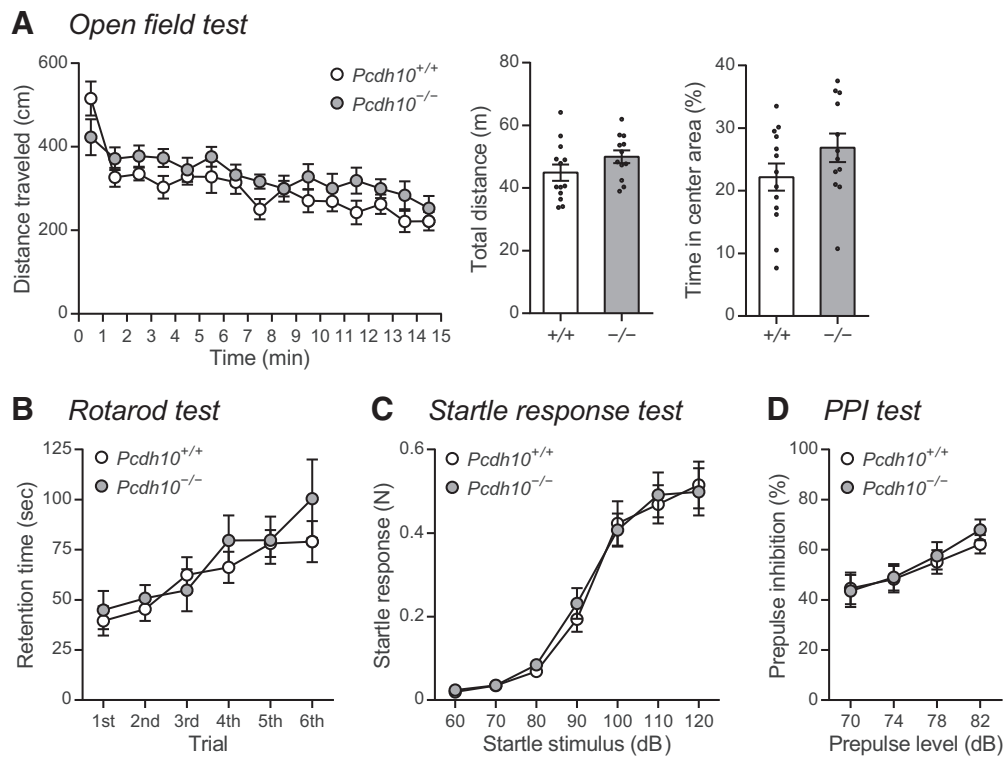


Figure 8. *Pcdh10* KO mice show normal sensory and motor behaviors. **A**, Open field test. The distance traveled during the 15-min test session, total distance, and time spent in the center area are similar between *Pcdh10*^{+/+} and *Pcdh10*^{-/-} mice. $n = 13$ mice for *Pcdh10*^{+/+} and 12 for *Pcdh10*^{-/-}. **B**, Rotarod test. The retention times through 6 trials are similar between *Pcdh10*^{+/+} and *Pcdh10*^{-/-} mice. $n = 13$ mice for *Pcdh10*^{+/+} and 12 for *Pcdh10*^{-/-}. **C**, Startle response test. Startle responses for different startle stimuli are similar between *Pcdh10*^{+/+} and *Pcdh10*^{-/-} mice. $n = 13$ mice for *Pcdh10*^{+/+} and 12 for *Pcdh10*^{-/-}. **D**, PPI test. PPI (%) by different prepulse levels are similar between *Pcdh10*^{+/+} and *Pcdh10*^{-/-} mice. $n = 13$ mice for *Pcdh10*^{+/+} and 12 for *Pcdh10*^{-/-}. Data are mean \pm SEM. Student's *t* test (**A–D**).

mouse line we have previously generated, which initially had a *LacZ/Neo* cassette, showed multiple brain abnormalities including axon defects; however, after removing the *LacZ/Neo* cassette, these abnormalities disappeared (Hoshina et al., 2013). Thus, we suggest our newly generated *Pcdh10* KO mouse line without the *LacZ/Neo* cassette reveal the actual functions of PCDH10: PCDH10 regulates synapse development, but not axon growth.

PCDH10-dependent excitatory synapse development

We found that PCDH10 is localized at synapses and regulates synapse development. In the BLA, PCDH10 is localized at VGLUT1-positive and VGLUT2-positive excitatory synapses as well as inhibitory synapses (Fig. 3D–H). Interestingly, *Pcdh10* KO mice showed differential effects on different types of synapses. For example, among excitatory synapses, VGLUT1-positive, but not VGLUT2-positive, synapses are affected in *Pcdh10* KO mice (Fig. 5). Thus, there is some specificity in terms of the roles of PCDH10 at synapses. Several synapse organizing molecules regulate synapse development in a synapse type-specific manner (Favuzzi and Rico, 2018; Sanes and Zipursky, 2020). Different fibroblast growth factors (FGFs) and neuropilins show differential effects on excitatory or inhibitory synapses (Graf et al., 2004; Chih et al., 2005; Terauchi et al., 2010). In addition, synapse organizing molecules may regulate synapses in a pathway-specific manner. Insulin-like growth factor 2 (IGF2) regulates the stabilization of the dentate gyrus-CA3 synapses, but not CA3-CA3 synapses (Terauchi et al., 2016). PCDH10 may be regulating synapses in the BLA both in a synapse type-specific and pathway-specific manner.

What might affect the specificity of PCDH10? An interesting regulator of PCDH10 is neural activity. The expression of

Pcdh10 is regulated by neural activity (Morrow et al., 2008). Therefore, PCDH10 might also regulate synapses in an activity-dependent manner. In a stable state (like in our experiments on synapses), PCDH10 might mainly regulate VGLUT1-positive excitatory synapses, but in certain situations, it may also regulate VGLUT2-positive excitatory synapses and inhibitory synapses. It would be interesting to test whether PCDH10 serves as a state-dependent regulator of synapses in the BLA.

It is also worth noting that at P14 (during synapse development), VGLUT1 puncta are only decreased in the dorsal BLA in *Pcdh10*^{-/-} mice (Fig. 5O); however, at P28 (at the end of synapse development), VGLUT1 puncta are decreased both in the dorsal and ventral BLA (Fig. 5F). Thus, defects in excitatory synapse development in the dorsal BLA may contribute to subsequent changes in other synapses in the BLA.

PCDH10 regulates dorsal BLA synapses and fear-related and anxiety-related behaviors

The amygdala controls fear and anxiety, and the BLA is the center for the input and output of such information (Tovote et al., 2015). The BLA integrates cortical, thalamic, hippocampal, and LA inputs and sends outputs to the central amygdala, which connects to various areas of the brain such as the PFC, hippocampus, and nucleus accumbens (NAc; Zhang et al., 2021). The BLA can be divided into the dorsal BLA and ventral BLA, which have different combinations of neuronal inputs and outputs (Hintiryan et al., 2021). Accordingly, the dorsal and ventral BLA control different aspects of emotional behaviors. Specifically, the dorsal BLA controls negative emotional behaviors such as fear-related behaviors and anxiety-related behaviors. In contrast, the ventral

BLA controls positive emotional behaviors such as reward-based behaviors (Kim et al., 2016; Yang and Wang, 2017; Beyeler et al., 2018). We found that PCDH10 is more highly expressed in the dorsal BLA than the ventral BLA (Fig. 3B) and regulates excitatory synapse development in the dorsal BLA (Fig. 5). Consistent with the role of the dorsal BLA in fear-related behaviors and anxiety-related behaviors, *Pcdh10* KO mice showed changes in fear conditioning and anxiety. PCDH10-positive synapses in the dorsal BLA may be the synapses responding to negative stimuli such as fear-related and anxiety-related signals and contributing to reducing anxiety and fear levels. Additionally, dorsal BLA neurons send outputs to the NAc and mPFC (Hintiryan et al., 2021), and these connections also regulate fear and anxiety behaviors (Zhang et al., 2021). Since PCDH10 is expressed in the NAc and mPFC as well, alterations in these connections may also contribute to the fear and anxiety phenotypes in *Pcdh10* KO mice.

Note that previously generated *Pcdh10*^{LacZ/Neo} heterozygous mice showed related but different behavioral phenotypes than our *Pcdh10* KO mice (Schoch et al., 2017; Ferri et al., 2021). We posit that the behavioral phenotypes of *Pcdh10*^{LacZ/Neo} heterozygous mice may reflect the roles of PCDH10-expressing neurons affected by the *LacZ/Neo* cassette, but may not reflect the exact role of PCDH10 per se

Involvement of PCDH10 in ASD, OCD, and MD

The human *PCDH10* gene has been linked to ASD, OCD, and MD (Morrow et al., 2008; Bucan et al., 2009; Qin et al., 2016; Roberson-Nay et al., 2020). The core symptoms of ASD include diminished social motivation, language problems, and restricted/repetitive behaviors (Kas et al., 2014). In rodent models, social interaction and social recognition tests assess sociability and social novelty preference, which are linked to social motivation. The USV test evaluates rodent social communication skills, which are related to language skills in humans. Rodent grooming and rearing behaviors are related to human restricted/repetitive behaviors. We found that *Pcdh10* KO mice show mild impairment in the social recognition test and USV test. Thus, PCDH10 appears to control social novelty preference and social communication skills. Mutations in *PCDH10* may lead to the impairment in such skills, exhibiting ASD-related symptoms.

Additionally, as described above, *Pcdh10* KO mice showed altered anxiety-related and fear-related behaviors. Abnormalities in anxiety and fear are frequently seen in ASD patients, and anxiety disorders and phobias often co-occur with ASD (Evans et al., 2005; White et al., 2009; Maddox and White, 2015; Postorino et al., 2017). OCD's symptoms include excessive anxiety and fear, and abnormal anxiety and fear are often seen in MD as well (Eysenck and Fajkowska, 2018; Stein et al., 2019). Panic disorder, phobia, anxiety disorder, and posttraumatic stress disorder are often comorbid with OCD and MD (Pallanti et al., 2011; Stein et al., 2019; Choi et al., 2020). Mouse models of ASD, OCD, and MD also exhibit abnormal anxiety-related and fear-related behaviors (Krishnan and Nestler, 2011; Alonso et al., 2015; Kazdoba et al., 2016). Mutations in *PCDH10* might alter the regulation of anxiety and fear, exhibiting symptoms related to ASD, OCD, and MD.

It is important to note that mutations found in *PCDH10* in human ASD are in the 3' region involved in the regulation of *PCDH10* expression (Morrow et al., 2008). Therefore, the mutations may either decrease or increase the expression of *PCDH10*. *Pcdh10* KO mice showed reduced anxiety and fear levels, phenotypes that are opposite to the excessive anxiety and fear levels associated with human psychiatric disorders. It is possible that

ASD mutations in *PCDH10* were increasing the expression of *PCDH10*, causing excessive anxiety and fear. As described above, the expression of *PCDH10* is regulated by neural activity. Thus, mutations in the 3' region of the *PCDH10* gene might also affect the activity-dependent regulation of *PCDH10*, which may result in altered anxiety, fear, and social motivation/communication.

Clinical implications

Our finding that the inactivation of *Pcdh10* in mice results in reduced anxiety and fear suggests that PCDH10 inhibition may help reduce excessive anxiety and fear in diseases. Currently, SSRIs and benzodiazepines are the most used anxiolytic drugs (Dunlop and Davis, 2008; Tan et al., 2011; Griffin et al., 2013; Stahl, 1998). However, both SSRIs and benzodiazepines have side effects such as insomnia, stomach upset, nausea, diarrhea (Ferguson, 2001), and addiction (Donoghue and Lader, 2010; Tan et al., 2011), causing some patients not to tolerate them. Our study suggests that PCDH10 could be a potential drug target for designing anxiolytics. Interestingly, *PCDH10* is implicated in SSRI-resistant OCD (Qin et al., 2016). Therefore, novel drugs targeting PCDH10 may be more effective than SSRIs for certain types of OCD and other psychiatric disorders.

References

- Alonso P, López-Solà C, Real E, Segalàs C, Menchón JM (2015) Animal models of obsessive-compulsive disorder: utility and limitations. *Neuropsychiatr Dis Treat* 11:1939–1955.
- Aoki E, Kimura R, Suzuki ST, Hirano S (2003) Distribution of OL-protocadherin protein in correlation with specific neural compartments and local circuits in the postnatal mouse brain. *Neuroscience* 117:593–614.
- Beyeler A, Chang CJ, Silvestre M, Lévêque C, Namburi P, Wildes CP, Tye KM (2018) Organization of valence-encoding and projection-defined neurons in the basolateral amygdala. *Cell Rep* 22:905–918.
- Bucan M, et al. (2009) Genome-wide analyses of exonic copy number variants in a family-based study point to novel autism susceptibility genes. *PLoS Genet* 5:e1000536.
- Chari T, Griswold S, Andrews NA, Fagiolini M (2020) The stage of the estrus cycle is critical for interpretation of female mouse social interaction behavior. *Front Behav Neurosci* 14:113.
- Chaste P, Leboyer M (2012) Autism risk factors: genes, environment, and gene-environment interactions. *Dialogues Clin Neurosci* 14:281–292.
- Chih B, Engelman H, Scheiffele P (2005) Control of excitatory and inhibitory synapse formation by neuroligins. *Science* 307:1324–1328.
- Choi KW, Kim YK, Jeon HJ (2020) Comorbid anxiety and depression: clinical and conceptual consideration and transdiagnostic treatment. *Adv Exp Med Biol* 1191:219–235.
- Cryan JF, Mombereau C, Vassout A (2005) The tail suspension test as a model for assessing antidepressant activity: review of pharmacological and genetic studies in mice. *Neurosci Biobehav Rev* 29:571–625.
- Detrait ER, Bowers WJ, Halterman MW, Giuliano RE, Bennice L, Federoff HJ, Richfield EK (2002) Reporter gene transfer induces apoptosis in primary cortical neurons. *Mol Ther* 5:723–730.
- Donoghue J, Lader M (2010) Usage of benzodiazepines: a review. *Int J Psychiatry Clin Pract* 14:78–87.
- Dunlop BW, Davis PG (2008) Combination treatment with benzodiazepines and SSRIs for comorbid anxiety and depression: a review. *Prim Care Companion J Clin Psychiatry* 10:222–228.
- Evans DW, Canavera K, Kleinpeter FL, Maccubbin E, Taga K (2005) The fears, phobias and anxieties of children with autism spectrum disorders and Down syndrome: comparisons with developmentally and chronologically age matched children. *Child Psychiatry Hum Dev* 36:3–26.
- Eysenck MW, Fajkowska M (2018) Anxiety and depression: toward overlapping and distinctive features. *Cogn Emot* 32:1391–1400.
- Favuzzi E, Rico B (2018) Molecular diversity underlying cortical excitatory and inhibitory synapse development. *Curr Opin Neurobiol* 53:8–15.

- Feng G, Mellor RH, Bernstein M, Keller-Peck C, Nguyen QT, Wallace M, Nerbonne JM, Lichtman JW, Sanes JR (2000) Imaging neuronal subsets in transgenic mice expressing multiple spectral variants of GFP. *Neuron* 28:41–51.
- Ferguson JM (2001) SSRI antidepressant medications: adverse effects and tolerability. *Prim Care Companion J Clin Psychiatry* 3:22–27.
- Ferri SL, Dow HC, Schoch H, Lee JY, Brodtkin ES, Abel T (2021) Age- and sex-specific fear conditioning deficits in mice lacking *Pcdh10*, an autism associated gene. *Neurobiol Learn Mem* 178:107364.
- Graf ER, Zhang X, Jin SX, Linhoff MW, Craig AM (2004) Neurexins induce differentiation of GABA and glutamate postsynaptic specializations via neuroligins. *Cell* 119:1013–1026.
- Griffin CE 3rd, Kaye AM, Bueno FR, Kaye AD (2013) Benzodiazepine pharmacology and central nervous system-mediated effects. *Ochsner J* 13:214–223.
- Hayashi S, Takeichi M (2015) Emerging roles of protocadherins: from self-avoidance to enhancement of motility. *J Cell Sci* 128:1455–1464.
- Hintiryan H, et al. (2021) Connectivity characterization of the mouse basolateral amygdalar complex. *Nat Commun* 12:2859.
- Hoshina N, Tanimura A, Yamasaki M, Inoue T, Fukabori R, Kuroda T, Yokoyama K, Tezuka T, Sagara H, Hirano S, Kiyonari H, Takada M, Kobayashi K, Watanabe M, Kano M, Nakazawa T, Yamamoto T (2013) Protocadherin 17 regulates presynaptic assembly in topographic cortico-basal ganglia circuits. *Neuron* 78:839–854.
- Hoshina N, Johnson-Venkatesh EM, Hoshina M, Umemori H (2021) Female-specific synaptic dysfunction and cognitive impairment in a mouse model of PCDH19 disorder. *Science* 372:eaz3893.
- Humeau Y, Reisel D, Johnson AW, Borchardt T, Jensen V, Gebhardt C, Bosch V, Gass P, Bannerman DM, Good MA, Hvalby Ø, Sprengel R, Lüthi A (2007) A pathway-specific function for different AMPA receptor subunits in amygdala long-term potentiation and fear conditioning. *J Neurosci* 27:10947–10956.
- Johnson-Venkatesh EM, Khan MN, Murphy GG, Sutton MA, Umemori H (2015) Excitability governs neural development in a hippocampal region-specific manner. *Development* 142:3879–3891.
- Kas MJ, Glennon JC, Buitelaar J, Ey E, Biemans B, Crawley J, Ring RH, Lajonchere C, Esclassan F, Talpos J, Noldus LP, Burbach JP, Steckler T (2014) Assessing behavioural and cognitive domains of autism spectrum disorders in rodents: current status and future perspectives. *Psychopharmacology (Berl)* 231:1125–1146.
- Kazdoba TM, Leach PT, Crawley JN (2016) Behavioral phenotypes of genetic mouse models of autism. *Genes Brain Behav* 15:7–26.
- Kim J, Pignatelli M, Xu S, Itoharu S, Tonegawa S (2016) Antagonistic negative and positive neurons of the basolateral amygdala. *Nat Neurosci* 19:1636–1646.
- Kimura S, Niwa H, Moriyama M, Araki K, Abe K, Miike T, Yamamura K (1994) Improvement of germ line transmission by targeting β -galactosidase to nuclei in transgenic mice. *Dev Growth Differ* 36:521–527.
- Krestel HE, Mihaljevic AL, Hoffman DA, Schneider A (2004) Neuronal co-expression of EGFP and beta-galactosidase in mice causes neuropathology and premature death. *Neurobiol Dis* 17:310–318.
- Krishnan V, Nestler EJ (2011) Animal models of depression: molecular perspectives. *Curr Top Behav Neurosci* 7:121–147.
- Lima Caldeira G, Peça J, Carvalho AL (2019) New insights on synaptic dysfunction in neuropsychiatric disorders. *Curr Opin Neurobiol* 57:62–70.
- Maddox BB, White SW (2015) Comorbid social anxiety disorder in adults with autism spectrum disorder. *J Autism Dev Disord* 45:3949–3960.
- Morrow EW, et al. (2008) Identifying autism loci and genes by tracing recent shared ancestry. *Science* 321:218–223.
- Müller U (1999) Ten years of gene targeting: targeted mouse mutants, from vector design to phenotype analysis. *Mech Dev* 82:3–21.
- Nakao S, Platek A, Hirano S, Takeichi M (2008) Contact-dependent promotion of cell migration by the OL-protocadherin-Nap1 interaction. *J Cell Biol* 182:395–410.
- Ouimet CC, Greengard P (1990) Distribution of DARPP-32 in the basal ganglia: an electron microscopic study. *J Neurocytol* 19:39–52.
- Pallanti S, Grassi G, Sarrecchia ED, Cantisani A, Pellegrini M (2011) Obsessive-compulsive disorder comorbidity: clinical assessment and therapeutic implications. *Front Psychiatry* 2:70.
- Pham CT, MacIvor DM, Hug BA, Heusel JW, Ley TJ (1996) Long-range disruption of gene expression by a selectable marker cassette. *Proc Natl Acad Sci U S A* 93:13090–13095.
- Port RG, Gajewski C, Krizman E, Dow HC, Hirano S, Brodtkin ES, Carlson GC, Robinson MB, Roberts TPL, Siegel SJ (2017) Protocadherin 10 alters γ oscillations, amino acid levels, and their coupling; baclofen partially restores these oscillatory deficits. *Neurobiol Dis* 108:324–338.
- Postorino V, Kerns CM, Vivanti G, Bradshaw J, Siracusano M, Mazzone L (2017) Anxiety disorders and obsessive-compulsive disorder in individuals with autism spectrum disorder. *Curr Psychiatry Rep* 19:92.
- Qin H, et al. (2016) Whole-genome association analysis of treatment response in obsessive-compulsive disorder. *Mol Psychiatry* 21:270–276.
- Redies C, Vanhalst K, Roy Fv (2005) delta-Protocadherins: unique structures and functions. *Cell Mol Life Sci* 62:2840–2852.
- Roberson-Nay R, Lapato DM, Wolen AR, Lancaster EE, Webb BT, Verhulst B, Hetttema JM, York TP (2020) An epigenome-wide association study of early-onset major depression in monozygotic twins. *Transl Psychiatry* 10:301.
- Sanes JR, Zipursky SL (2020) Synaptic specificity, recognition molecules, and assembly of neural circuits. *Cell* 181:536–556.
- Schoch H, et al. (2017) Sociability deficits and altered amygdala circuits in mice lacking *Pcdh10*, an autism associated gene. *Biol Psychiatry* 81:193–202.
- Sorra KE, Harris KM (2000) Overview on the structure, composition, function, development, and plasticity of hippocampal dendritic spines. *Hippocampus* 10:501–511.
- Stahl SM (1998) Mechanism of action of serotonin selective reuptake inhibitors. Serotonin receptors and pathways mediate therapeutic effects and side effects. *J Affect Disord* 51:215–235.
- Stein DJ, Costa DLC, Lochner C, Miguel EC, Reddy YCJ, Shavitt RG, van den Heuvel OA, Simpson HB (2019) Obsessive-compulsive disorder. *Nat Rev Dis Primers* 5:52.
- Tan KR, Rudolph U, Lüscher C (2011) Hooked on benzodiazepines: GABAA receptor subtypes and addiction. *Trends Neurosci* 34:188–197.
- Terauchi A, Johnson-Venkatesh EM, Toth AB, Javed D, Sutton MA, Umemori H (2010) Distinct FGFs promote differentiation of excitatory and inhibitory synapses. *Nature* 465:783–787.
- Terauchi A, Johnson-Venkatesh EM, Bullock B, Lehtinen MK, Umemori H (2016) Retrograde fibroblast growth factor 22 (FGF22) signaling regulates insulin-like growth factor 2 (IGF2) expression for activity-dependent synapse stabilization in the mammalian brain. *Elife* 5:e12151.
- Terauchi A, Gavin E, Wilson J, Umemori H (2017) Selective inactivation of fibroblast growth factor 22 (FGF22) in CA3 pyramidal neurons impairs local synaptogenesis and affective behavior without affecting dentate neurogenesis. *Front Synaptic Neurosci* 9:17.
- Toro R, Konyukh M, Delorme R, Leblond C, Chaste P, Fauchereau F, Coleman M, Leboyer M, Gillberg C, Bourgeron T (2010) Key role for gene dosage and synaptic homeostasis in autism spectrum disorders. *Trends Genet* 26:363–372.
- Tovote P, Fadok JP, Lüthi A (2015) Neuronal circuits for fear and anxiety. *Nat Rev Neurosci* 16:317–331.
- Tsai NP, Wilkerson JR, Guo W, Maksimova MA, DeMartino GN, Cowan CW, Huber KM (2012) Multiple autism-linked genes mediate synapse elimination via proteasomal degradation of a synaptic scaffold PSD-95. *Cell* 151:1581–1594.
- Uemura M, Nakao S, Suzuki ST, Takeichi M, Hirano S (2007) OL-Protocadherin is essential for growth of striatal axons and thalamocortical projections. *Nat Neurosci* 10:1151–1159.
- Umemori H, Linhoff MW, Ornitz DM, Sanes JR (2004) FGF22 and its close relatives are presynaptic organizing molecules in the mammalian brain. *Cell* 118:257–270.
- White SW, Oswald D, Ollendick T, Scahill L (2009) Anxiety in children and adolescents with autism spectrum disorders. *Clin Psychol Rev* 29:216–229.
- Williams AJ, Yee P, Smith MC, Murphy GG, Umemori H (2016) Deletion of fibroblast growth factor 22 (FGF22) causes a depression-like phenotype in adult mice. *Behav Brain Res* 307:11–17.
- Yang Y, Wang JZ (2017) From structure to behavior in basolateral amygdala-hippocampus circuits. *Front Neural Circuits* 11:86.
- Zhang WH, Zhang JY, Holmes A, Pan BX (2021) Amygdala circuit substrates for stress adaptation and adversity. *Biol Psychiatry* 89:847–856.
- Zhu XN, Liu XD, Sun S, Zhuang H, Yang JY, Henkemeyer M, Xu NJ (2016) Ephrin-B3 coordinates timed axon targeting and amygdala spinogenesis for innate fear behaviour. *Nat Commun* 7:11096.